Order Number 1357426

A novel beam-assisted thickness measurement technique for nanostructures

Casas, Luis Manuel, M.S.

New Jersey Institute of Technology, 1994

U·M·I
300 N. Zeeb Rd.
Ann Arbor, MI 48106

ABSTRACT

A NOVEL BEAM-ASSISTED THICKNESS MEASUREMENT TECHNIQUE FOR NANOSTRUCTURES

by
Luis Manuel Casas

A novel method for measuring thickness of thin films has been developed. This method is straightforward, quickly accomplished, and offers resolution of device layers approaching that given by transmission electron microscopy. Ion beam bombardment of a multi-layer structure forms a crater in which the crater sidewalls are beveled at a very shallow angle, revealing various layers within the sample at a high degree of magnification. Beveled film thicknesses are measured by scanning Auger electron spectroscopy. Depth profilometry is used to measure the shallow beveling angle. Through knowledge of the beveled layer thickness and the bevel angle, actual film thicknesses are easily calculated. For structures in which delineation of distinct layers is difficult, chemical etching enhances features on the beveled crater sidewall, enabling resolution of layers as thin as 20Å.

A NOVEL BEAM-ASSISTED THICKNESS MEASUREMENT TECHNIQUE FOR NANOSTRUCTURES

by
Luis Manuel Casas

A Thesis
Submitted to the Faculty of
New Jersey Institute of Technology
in Partial Fulfillment of the Requirements for the Degree of
Master of Science in Electrical Engineering

Department of Electrical and Computer Engineering

May 1994

APPROVAL PAGE

A NOVEL BEAM-ASSISTED THICKNESS MEASUREMENT TECHNIQUE FOR NANOSTRUCTURES

Luis Manuel Casas

Dr. N.M. Ravindra, Thesis Advisor — Date
Associate Professor of Physics, NJIT

Dr. Richard T. Lareau, Thesis Advisor — Date
Leader, Device Microanalysis Team
Army Research Laboratory - Electronics and Power Sources Directorate

---

Dr. Walter F. Kosonocky, Committee Member — Date
Sponsored Chair and Professor of Optoelectronics, NJIT

Dr. Kenneth S. Sohn, Committee Member — Date
Acting Chairman and Professor of Electrical and Computer Engineering, NJIT

BIOGRAPHICAL SKETCH

Author: Song Chen

Degree: Doctor of Philosophy

Date: May 1995

Undergraduate and Graduate Education:

- Doctor of Philosophy in Computer Science,
  New Jersey Institute of Technology, Newark, New Jersey, 1995
- Master of Science in Systems Engineering,
  Shanghai Jiao Tong University, Shanghai, P. R. China, 1990
- Bachelor of Science in Computer Science,
  East China Normal University, Shanghai, P. R. China, 1987

Major: Computer Science

Presentations and Publications:

S. Chen and M. M. Eshaghian, "A Fast Recursive Mapping Algorithm," to appear in Concurrency: Practice and Experience, August 1995.

S. Chen, M. M. Eshaghian, R. F. Freund, J. L. Potter, and Y. Wu, "Evaluation of Two Programming Paradigms for Heterogeneous Computing," to appear in Journal of Parallel and Distributed Computing, 1995/1996.

S. Chen, M. M. Eshaghian, and Y. Wu, "Mapping Arbitrary Non-Uniform Task Graphs onto Arbitrary Non-Uniform System Graphs," submitted to IEEE Transactions on Parallel and Distributed Computing.

S. Chen and M. M. Eshaghian, "Tools for Design and Mapping of Portable Parallel Programs," to appear in Proceedings of Workshop on Challenges for Parallel Processing, International Conference on Parallel Processing, August 1995.

S. Chen, M. M. Eshaghian, and Y. Wu, "Mapping Arbitrary Non-Uniform Task Graphs onto Arbitrary Non-Uniform System Graphs," to appear in Proceedings of International Conference on Parallel Processing, August 1995.

S. Chen, M. M. Eshaghian, R. F. Freund, J. L. Potter, and Y. Wu, "Scalable Heterogeneous Programming Tools," Proceedings of Heterogeneous Computing Workshop, pp 89-96, April 1994.

This thesis is dedicated to my mother and father, who always dreamed their children would exceed all their aspirations.

ACKNOWLEDGMENT

The author wishes to express sincere thanks to his supervisors, Professor N.M. Ravindra and Dr. Richard T. Lareau, for their guidance and support throughout this research effort.

Special thanks to Professors Walter F. Kosonocky and Kenneth S. Sohn for serving as committee members.

Very special thanks to Donald W. Eckart for invaluable assistance in performance of experiments and providing insight into phenomena comprising this research.

Thanks to Daniel E. Pierce for enlightening discussions and ideas throughout this research.

Thanks to Melanie W. Cole for providing TEM measurements and productive discussions during the course of this research.

Thanks to Stephen N. Schauer, Andrew E. Souzis, and Timothy P. Monahan for providing support and incentive throughout this research, especially during times of uncertainty in research efforts.

TABLE OF CONTENTS

LIST OF TABLES

LIST OF FIGURES

LIST OF FIGURES
(continued)

LIST OF FIGURES
(continued)

Figure **Page**

CHAPTER 1

THESIS ORGANIZATION

This thesis is comprised of the research work performed in development of the technique of measuring film thicknesses through shallow angle beveling of multi-layer structures with an ion beam. Chapter 1 lists the organization of the thesis. Chapter 2 documents relevant background material and provides the motivation for this study. Chapter 3 describes the experimental procedures used in measuring all parameters associated with the shallow angle beveling phenomenon. Chapter 4 presents the results and interpretation of the investigation. This is the most substantial portion of the thesis, as a variety of materials systems have been studied. Chapter 5 states the conclusion of this research and briefly outlines related future work. Issues requiring further study are noted, along with ideas for methods of addressing these issues.

CHAPTER 2

BACKGROUND

Miniaturization of device structures has been a trend in electronic and optoelectronic device technology [1]. In both Si and GaAs technology, field effect transistors (FETs) with a gate length of 0.5 μm are routinely manufactured [2,3]. Furthermore, FETs with a gate length of 0.1 μm have been successfully fabricated [4]. This reduction in device size offers desirable properties such as increased device packing density and superior frequency response [1]. As lateral device dimensions become smaller, the thicknesses of multi-layer structures must be appropriately scaled down. In Si technology, a 0.3 μm gate length metal oxide semiconductor field effect transistor (MOSFET) requires an SiO_2 insulating layer with a thickness of approximately 60Å [5]. Prototype MOSFETs with a gate length of 0.1 μm require the thickness of the SiO_2 insulating layer to be no more than 30-35Å [6]. In GaAs microwave device technology, a pseudomorphic high electron mobility transistor (p-HEMT) requires an electrically active region (typically InGaAs) with a thickness of approximately 100Å [7]. AlGaAs/GaAs multiple quantum well (MQW) superlattices have been fabricated for infrared detector applications in which the thickness of alternating GaAs layers is typically less than 100Å [8]. In addition, AlGaAs/GaAs superlattice layers are grown on a GaAs substrate as a buffer layer to provide a smooth surface for subsequent active layer growth [9]. The thickness of the GaAs layers within the superlattice may be as thin as 20Å.

In order to characterize the electrical and optical properties of such devices, film thicknesses need to be measured as accurately as possible. In a p-HEMT, nearly all electrical properties used to evaluate device performance are dependent upon accurate assessment of the mole fraction of the InGaAs active

region and thickness of the InGaAs layer [10]. Optical and optoelectronic devices generally require multiple layers of precise thickness in order to yield specific refractive indices or impedance matching characteristics [11]. In order to properly determine materials and device characteristics, a simple technique for measuring the thickness of thin films is required.

A variety of techniques for measuring film thickness are readily available. However, they all suffer from certain limitations. Commercial stylus depth profilometry instruments cannot reliably measure the thickness of very thin films. When attempting to measure thicknesses less than 100Å, these instruments are limited by susceptibility to vibration during measurement and surface roughness introducing uncertainty in the data [12]. Single wavelength and spectroscopic ellipsometers are also available for thickness measurements. These instruments can accurately measure thicknesses on the order of ~100Å, but are limited in that a priori knowledge of the structure is necessary to accurately assess film thickness [13]. If the true sample composition agrees with nominal device design, then the indices of refraction of respective layers are well known and hence, meaningful thickness measurements may be derived. But, if the sample composition differs from the nominal design, assumed refractive indices are no longer valid and associated thickness measurements are suspect. Parametric fluctuations during film growth processes such as molecular beam epitaxy (MBE) or chemical vapor deposition (CVD) may result in compositional variations within multi-layer structures [14], rendering thicknesses derived by ellipsometry to be inaccurate. Furthermore, post-growth processing such as conventional annealing or rapid thermal annealing (RTA) often results in chemical alloying between adjacent films or elemental/ionic migration between films [15]. In such cases, use of ellipsometry to measure film thicknesses is not viable. Transmission electron microscopy (TEM) is the time-honored method for

measuring thickness of thin films [16]. TEM is accurate to ± 2Å and yields an unambiguous crystallographic representation of multi-layer device structures. However, TEM is very expensive and time-consuming [17]. Sample preparation for TEM involves excessive grinding and polishing of the specimen to be analyzed, as well as an ion milling procedure to properly thin the sample. The entire process is lengthy and tedious.

There is a need to develop a technique for measuring thin film thicknesses which is straightforward, quickly accomplished and offers resolution approaching that of TEM analysis [17]. Through ion beam bombardment of a multi-layer structure, a crater is formed in which the crater sidewalls are observed to be beveled. In effect, the ion beam bevels the sample, revealing the various layers within the sample and their respective interfaces. Furthermore, this beveling phenomenon occurs at an extremely shallow angle. This serves to not only reveal the multiple layers, but also greatly magnify them so that beveled film thicknesses may be easily measured. Observation of the beveled structure is performed through scanning electron microscopy (SEM). In cases where adjacent films have similar composition, interfacial delineation is difficult [12]. By subjecting the sample to a suitable chemical etch, resolution of adjacent films is possible. Scanning Auger electron spectroscopy is used to accurately measure the beveled layer thickness. Mechanical stylus depth profilometry is used to measure the shallow beveling angle. By knowing the beveled layer thickness and the beveling angle, actual film thickness may be easily calculated. The technique is very simple and straightforward. Film thicknesses on the order of 100Å may be measured, and films as thin as 20Å may be resolved. Despite the fact that the technique is destructive, it is localized to a small area (as small as 50 μm x 50 μm square). Thus a very small region is consumed in the analysis. This offers a powerful technique for monitoring wafer fabrication at successive stages. Test

pads incorporated onto processed wafers may be probed so that multi-layer structures may be analyzed without destroying actual devices. Multiple measurements may be performed across an entire wafer of device prototypes. The method may be used for lateral uniformity studies of films deposited by MBE or CVD. Interdiffusion between deposited layers due to wafer processing may be visually and quantitatively studied. The technique has been performed using a scanning Auger microprobe, but may be accomplished using other surface analysis techniques employing ion beam sputtering such as secondary ion mass spectrometry (SIMS) [18] or X-ray photoelectron spectroscopy (XPS) [19]. When used in conjunction with these forms of analysis, the technique is powerful in that chemical analysis of beveled layers is possible. Thus, unknown or ambiguous beveled layers may be probed and chemically identified. In short, this shallow angle beveling technique provides measurement of film thicknesses as thin as ~ 100Å in a relatively short time. Hence, there is a great utility for such a technique in the characterization of electronic and optoelectronic multi-layer structures and devices.

CHAPTER 3

EXPERIMENTAL METHODS

3.1 Auger Electron Spectroscopy

For this research, beveled sputter craters are created using Ar^+ ion beams in a Perkin-Elmer PHI660 scanning Auger microprobe with a scanning electron microscope attachment (SAM/SEM). This is a commercial system for performing Auger electron spectroscopy (AES). A general schematic of the system is given in figure 3.1. The system is equipped with a high-energy electron gun which stimulates Auger transitions within the analyzed sample. Typical electron beam voltages vary between 5-15 kV. The electron source is a lanthanum hexaboride (LaB_6) filament which can be finely focused to a beam diameter of ~500Å. A cylindrical mirror analyzer (CMA) is mounted coaxially around the electron gun filament. The CMA is the energy spectrometer which records the electron

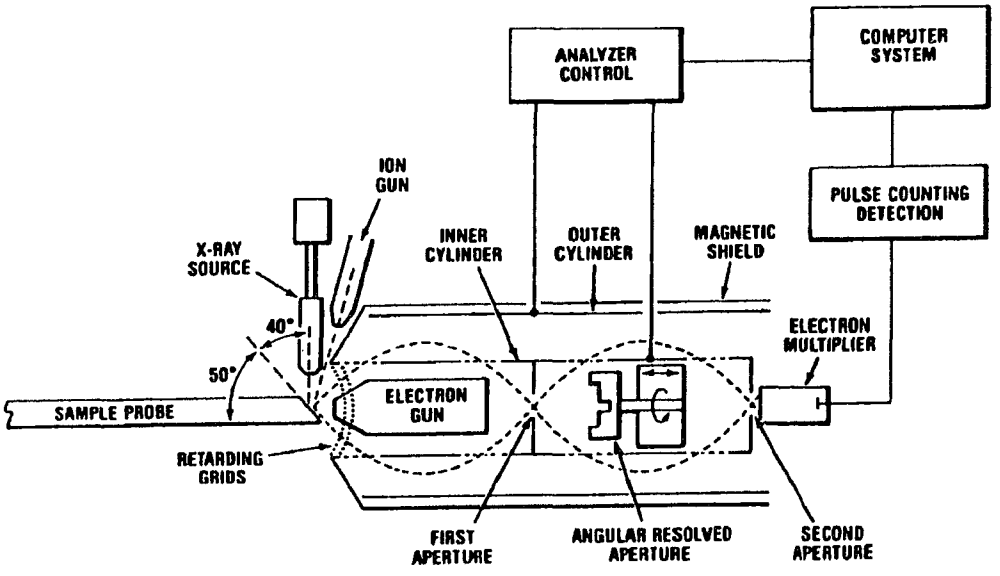

Figure 3.1 General schematic of scanning Auger microprobe (SAM) (Courtesy of Physical Electronics Industries, Inc.)

energy. The CMA is normally scanned over the energy range of 30 eV-2200 eV [20], since nearly all Auger electronic transitions occur within this range. The detected signal is subsequently amplified by an electron multiplier and stored on a graphics-intensive workstation. The system is fully automated, with all system electronics being computer-controlled through a sophisticated data acquisition software package. It is to be noted that the X-ray source in figure 3.1 is an attachment to the system. The PHI660 used in this research work contains no X-ray source.

In the most basic mode of operation, the result of this analysis is an energy spectrum in which the number of detected secondary electrons N(E) is plotted as a function of electron kinetic energy E. Auger electrons are observed as small superimposed signals upon a large background of secondary electron signal. The small intensity of the Auger signal residing on a much larger background of secondary electron signal renders elemental identification uncertain in analyzing the N(E) vs. E spectrum. To facilitate the analysis, the N(E) signal is numerically differentiated with respect to kinetic energy. The resulting dN(E)/dE vs. E spectrum magnifies the Auger signal over the contiguous background such that elemental identification is simplified considerably. Figure 3.2 is an example of a differentiated energy spectrum of stainless steel. The peak structure of the differentiated signal is readily identifiable. In addition, the peak-to-peak intensity of the differentiated Auger signal is directly proportional to elemental atomic concentration [21]. Thus, through application of suitable proportionality factors known as relative sensitivity factors (RSFs) [21], quantitative information may be derived by AES. Due to variations in Auger electron escape depth and ionization cross section in different material systems, RSF values for a particular Auger transition may differ considerably among samples [21]. This uncertainty in RSF proportionality factors limits quantitation by AES to a

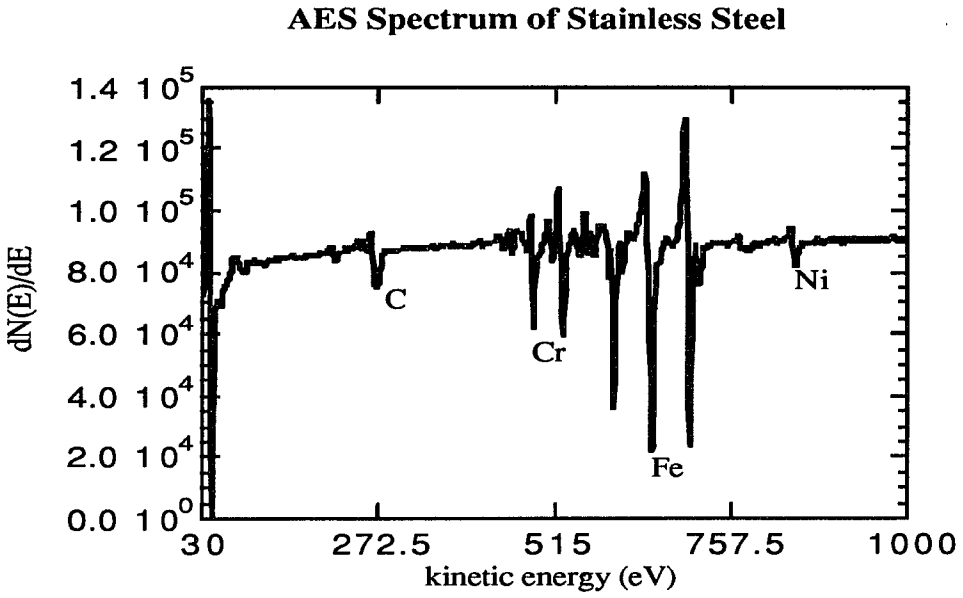

Figure 3.2 Auger energy spectrum of stainless steel

modest approximation of true sample composition, typically ± 30-40% at. Of course, this semi-quantitative analysis is accomplished without the use of sample standards. Highly accurate quantitative analysis by AES may be achieved through the use of a standard in which composition is well known [20]. Preliminary analysis of the standard enables calibration of the RSF value associated with an Auger transition. Once the RSF value is precisely determined, the sample of interest is analyzed and the predetermined RSF value is applied to the Auger signal in the test sample. Through this method, accurate quantitation is possible. Such a protocol for materials characterization is common in surface analysis, most notably for the technique of secondary ion mass spectrometry (SIMS) [22].

The PHI660 AES system is also equipped with a duoplasmatron ion source for sputter-etching the sample surface. It is the ion beam which produces the sputter crater in which the sidewalls are beveled. Semiconductor grade

(99.999% pure) argon gas is introduced into the system and promptly ionized by an electrical discharge. During the discharge, the ion source cathode is held at high voltage and the anode, located at an intermediate point between the cathode and sample, is maintained at ground potential. Subsequently, the Ar^+ ions are accelerated down the microbeam ion column and bombard the sample at a focused spot. For typical sputtering conditions, the Ar^+ beam diameter is 20-40 μm. Typical accelerating potential and sample target current are 2-4 kV and 5-500 nA respectively. The angle of incidence of the beam may be varied from 0-80° measured with respect to sample normal. For most applications, the Ar^+ beam is incident at an angle of 50° with respect to sample normal. The beam is electronically rastered in a square x-y pattern to erode the surface evenly. By sputter-etching the sample surface and acquiring AES data, elemental variations as a function of depth may be probed. This is known as an AES intensity depth profile. This mode of acquisition differs from the spectral analysis previously discussed in that data is obtained in a multiplexing fashion. Numerous elements may be monitored in one depth profile. Specific Auger transitions within discrete energy windows are monitored during the analysis. For example, the oxygen KLL Auger transition is characterized by a differentiated signal in which the maximum occurs at an energy of 504 eV and the minimum at 511 eV [23]. Hence, a window of 492-520 eV is monitored and the peak-to-peak intensity of the Auger signal is recorded. This process occurs for all elements monitored during each acquisition cycle. Two pre-sputter cycles occur in which Auger data is acquired before etching commences. This is performed in order to probe the surface region without disturbing the sample by high-energy Ar^+ bombardment. With the onset of sputtering, data acquisition may proceed in one of two modes. In the continuous sputtering mode, Auger data is recorded while the Ar^+ beam simultaneously sputters the sample. In the alternating sputtering

mode, the analysis cycles back and forth between sputtering and data acquisition. No sputtering occurs while Auger data is being recorded. The former is ideal for quick analysis of relatively thick (~1 μm) films, but suffers from degradation in depth resolution. The latter is more time consuming, but results in optimum depth resolution for thin films. Choice of acquisition mode is application-dependent. Figure 3.3 is an example of a depth profile analysis. The sample is a prototype Pt/Ti Ohmic contact to GaAs. Data is acquired in the alternating sputter mode. The plot is fairly self-explanatory. Beginning at sputter time t=0, the Pt surface layer is detected. At time t=7 minutes, the Pt layer is sputtered away and the Ti layer is detected. Subsequently at time t=14 minutes, the Ti layer is etched away and the GaAs substrate is detected. The result is multiple Auger peak-to-peak signal intensities plotted as a function of sputter time. By applying the RSF values previously discussed to each signal, the signal intensity depth profile may be converted into an atomic concentration (AC) depth profile in which elemental concentration is plotted vs. sputter time.

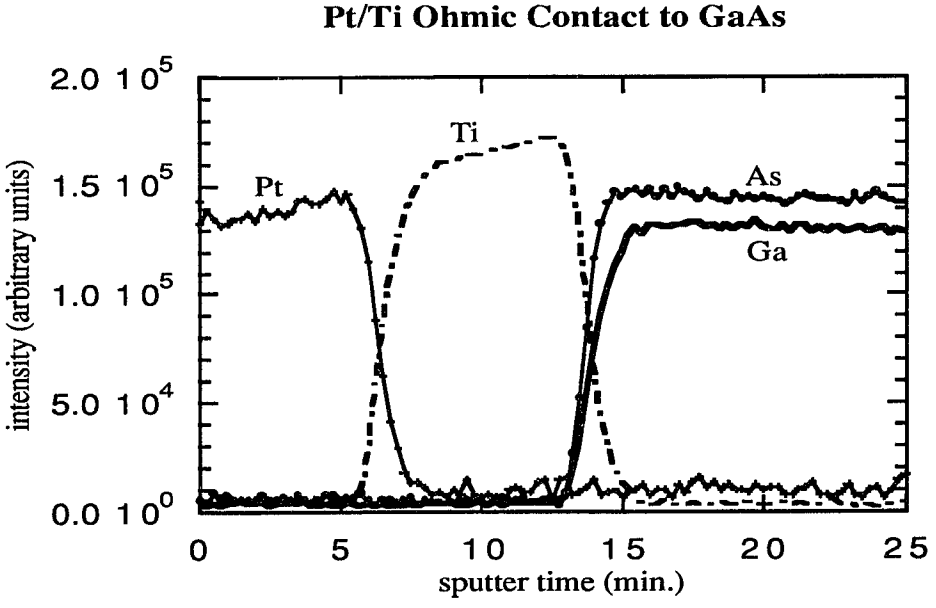

Figure 3.3 Auger depth profile of Pt/Ti Ohmic contact

In addition, through knowledge of material sputter rates or independent depth measurements by stylus depth profilometry, a depth scale may be assigned to the data in order to replot elemental concentration as a function of sample depth [24], the most meaningful representation of the acquired data. In this way, the dependence of elemental distribution with depth may be suitably probed.

The system also contains a secondary electron detector which amplifies and sends output signals to a cathode ray tube (CRT). This effectively acts as a scanning electron microscope (SEM) for imaging of samples. The system is optimized to collect Auger data, but not for high resolution imaging. In considering optimization of both lateral resolution and data acquisition conditions, a trade-off exists between quality AES data and high lateral resolution in the system. To optimize statistical precision of Auger data, the signal-to-noise (S/N) ratio should be maximized. In order to accomplish this, analysis is performed using the maximum amount of electron target current possible without damaging the sample surface through excessively high current density. As the electron current is increased, the beam diameter experiences a corresponding increase. This increase in beam size results in degradation of lateral resolution in the SEM image. Thus, choice of experimental parameters is application-dependent. Statistical validity of Auger data is optimized at the expense of lateral resolution. Likewise, while imaging capability is improved, Auger signals grow weaker and the S/N ratio decreases dramatically. Applications requiring both statistically acceptable data and relatively high lateral resolution involve fine tuning of experimental parameters in order to satisfy analysis specifications. In short, acquiring Auger data at maximum S/N ratio and minimum electron beam diameter is mutually exclusive. This is generally true for LaB_6 electron beam sources and older W sources [20]. The latest AES instruments manufactured employ field emission electron sources

which bridge the two extremes [25]. The physical principles behind operation of field emission sources dictate that high S/N ratio may be achieved without sacrificing lateral resolution. This is due to increased electron beam flux obtained in field emitters [25]. In conclusion, despite limitations in lateral resolution of the SAM relative to stand-alone SEM systems, formation of the beveled crater and measurement of multi-layer structures may be performed in-situ. This is quite desirable, since otherwise measurement of the beveled layers with a stand-alone SEM would require removing the sample from the system chamber and breaking vacuum. This would result in the sample surface becoming contaminated with oxygen and hydrocarbons from the atmosphere [24]. Rather than attempting to measure the thickness of beveled films on a surface which is subject to contamination, it is best to perform thickness evaluations on a pristine surface under vacuum.

Regarding vacuum conditions, the system is operated under ultra-high vacuum (UHV). The main chamber is pumped by an ion pump. In addition, Ti sublimators are incorporated to maintain excellent vacuum. The ion gun source assembly and the load-locked sample introduction station are both maintained under UHV by turbomolecular pumps. Base pressure is approximately 7E-11 Torr. Typical operating pressure is ~ 1E-10 Torr without ion gun operation, and ~ 5E-08 Torr with the ion gun in use. Ion gun operation results in higher system pressure due to a constant flow of Ar gas into the differentially pumped ion source. The requirement of UHV ambient during analysis is essential to maintain elemental background signals at a suitably low level and to eliminate analytical artifacts caused by electron scattering from residual background gases [19]. In defining an acceptable background level, the sensitivity of the AES technique must be considered. Under optimum conditions, the limit of detection (LOD) of AES is 0.1-0.5% at. [21]. In worst cases in which the signal is quite noisy, the

LOD may be several atomic percent. AES is limited in this respect relative to other chemical characterization techniques. Detection limits of parts-per-million to parts-per-billion may be achieved in secondary ion mass spectrometry (SIMS) [12]. Sensitivities of parts-per-trillion have been reported using glow discharge mass spectrometry (GDMS) [26]. Since the Auger technique is characterized by much more modest sensitivity, suitable background gas levels are attained more easily. For example, during an AES analysis, a contaminant gas present within the chamber at a concentration in the parts-per-million range will not be detected at all. This same gas will cause a detectable signal background during SIMS analysis. The most problematic contaminant elements in AES analysis are carbon and oxygen. Large C and O signals are always detected at the sample surface prior to sputter cleaning. With the onset of sputtering, both signals are observed to disappear. The C and O are detected on the surface from atmospheric contamination. C and O are reactive gases which bond to the surfaces of nearly all materials. For example, Si will form a native oxide simply from being exposed to atmospheric oxygen [20]. The fact that the C and O signals vanish with the onset of sputtering indicates that the presence of these elements are due to surface contamination and not system background. In short, due in part to low detection limits, a UHV system effectively eliminates nearly all elemental backgrounds in Auger analysis.

Craters featuring beveled sidewalls are generated during Auger depth profiling. For the purpose of creating the beveled crater, Auger analysis is not essential. The only requirement is the ion beam bombardment of the sample. Nevertheless, the analysis is useful in that it enables correlation of chemically-identified layers with layers observed via SEM or optical microscopy. Illustrative results of this work are presented in the next chapter of this report. The beveling phenomenon appears to be independent of ion current density.

Increased current density results in an increased sputter-etch rate. Therefore, increased ion current flux results in the beveling proceeding more quickly. However, this increase degrades the depth resolution of associated Auger data acquired during the analysis [21]. These are competing processes, and a trade-off exists between analysis time and detailed resolution of Auger data. It is possible to optimize the procedure to yield satisfactory chemical results in a reasonable amount of time. Variation of these parameters is application-dependent. If Auger chemical data is unimportant, the beveling process may be completed in 5-10 minutes. But in order to correlate chemical and structural data, it is advantageous to increase analysis time in order to increase depth resolution of chemical data. Through this methodology, an optimum operating point is determined.

At optimum focus, the Ar^+ ion beam should theoretically resemble a three-dimensional Gaussian distribution [20]. A plot of ion current density as a function of position should yield a Gaussian curve. Extension of such a plot to three dimensions results in a three-dimensional Gaussian volume with a current density maximum at the center of the beam. The beam may be optimally focused such that the full-width half-maximum of the beam encompasses a laterally circular area of radius ~ 20 μm. As the beam rasters a small area to form a sputter crater, the crater sidewalls are generated by the tail of the beam. Since the physical beam shape is that of a three-dimensional Gaussian distribution, the Ar^+ current density is greatest at the center of the beam and less at the beam edge. This decreased ion current density at the beam tail causes material subjected to the beam tail to be eroded less rapidly than that which is subjected to the center of the beam. That is, the crater sidewalls are sputtered more slowly than the central portion of the crater. As position is varied within the ion beam, the sputter rate increases as one approaches the center of the beam. It is this very

fact which results in the crater sidewalls being effectively beveled, revealing the various layers within the device structure at a high degree of magnification. At sufficiently shallow bevel angles, which results in increased layer magnification, beveled layers may be easily detected via SEM.

Upon completion of the analysis, the crater with beveled sidewalls is formed. The next step is measurement of the beveled layer thicknesses. With SEM capability, layer thicknesses may be measured, but not to the desired accuracy. An alternate approach is the use of Auger line scan data acquisition [21]. On the SEM field of view, the electron beam is swept in a horizontal or vertical line, scanning for specific elements throughout. The scan resolution may be set at a maximum of 512 pixels per line. The thickness of the line is ultimately the electron beam diameter. Like the depth profiling analysis previously discussed, data is acquired in a multiplexing mode. Specific energy windows in which definite Auger transitions occur are monitored. Determining particular elemental windows to be scanned requires prior knowledge of sample structure. However, the initial depth profile analysis resulting in the shallow crater sidewalls predetermines elemental species present within the sample. Thus elements to be monitored during Auger line scan analysis are defined. The result of such analysis is a plot of elemental signal intensity as a function of position in the SEM field of view. Figure 3.4 is an example of an AES line scan of Al along the beveled sidewall of a prototype pseudomorphic high electron mobility transistor (p-HEMT) device structure. The device consists of GaAs, AlGaAs, and InGaAs layers of varying thicknesses. No Al is detected in the region prior to approximately 18 μm. This corresponds to a GaAs layer. The signal then rises and quickly falls off, corresponding to an AlGaAs layer. The signal rises once again and periodically fluctuates. Here the presence of the AlGaAs(200Å)/GaAs(18Å) superlattice is detected. The resolution is such that

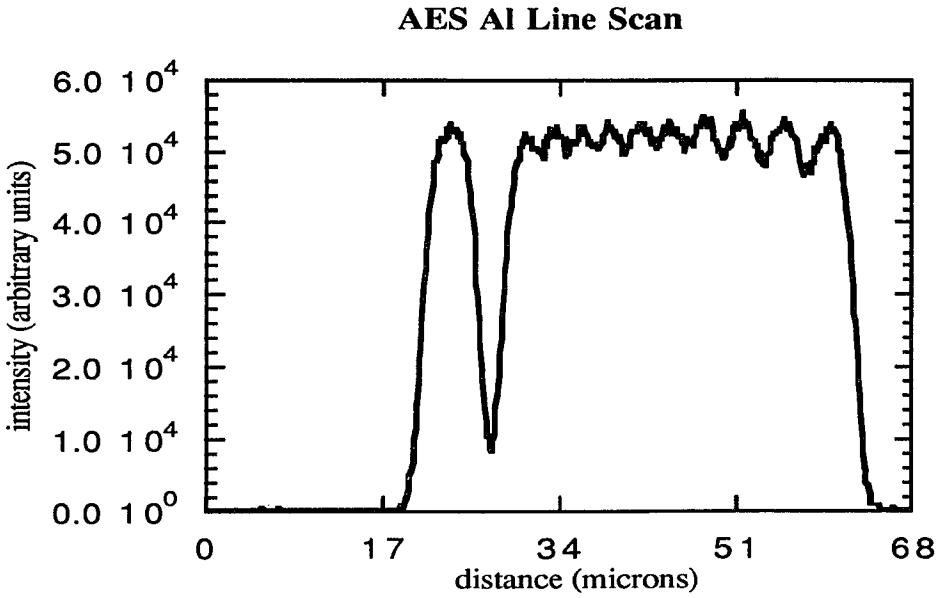

Figure 3.4 Auger line scan of Al along sidewall of p-HEMT

each of ten superlattice periods is observed. By using a predefined signal point as to the beginning and ending of a layer, the beveled thickness of the layer in question may be readily measured. The limitation of the analysis is the size of the electron beam. Generally when measuring film thicknesses, the size of the electron beam probing the film should be as small as possible. But from previous discussions, a minimally small electron beam results in a little to no Auger signal being generated. In order to detect acceptable signal levels, beam size must necessarily be sacrificed. Thickness measurements are still possible, provided that the beam size does not approach the film thickness being measured. In present experiments, in cases when the electron beam diameter is measured to be approximately one-fifth the size of the film thickness being probed, measured thicknesses are consistent with nominal values or actual thickness values derived by transmission electron microscopy (TEM). A significantly larger beam may introduce error into the measurements.

Results of the Auger line scan enable measurement of beveled layer thicknesses. However, the plot does not visually show the characteristics of the beveled layers. A pictorial representation of the analysis crater is valuable in order to see the beveled sidewalls, possibly lending insight into the ion beam beveling phenomenon. In addition, an image of the sidewalls provides qualitative uniformity information in that the beveled layers may be observed over relatively large distances. Typical analysis craters are formed over a 200 μm x 200 μm region. Thickness fluctuations in beveled layers may be visually inspected over this region, obtaining insight into the lateral uniformity of deposited films. If adjacent layers in the beveled multi-layer structure are sufficiently different in composition, all layers are visible along the sidewalls by SEM [12]. An SEM micrograph of the analysis crater shows the beveled sidewalls and all respective device layers. However, layers which are similar in composition are difficult to distinguish by SEM. In such instances, distinct layers may be resolved through Auger surface map analysis [20]. Like AES line scans, this type of measurement monitors Auger elemental transitions at the sample surface throughout the field of view of the SEM. Data is acquired in a multiplexing mode. Auger surface map analysis may be thought of as a sequential series of horizontal line scans across the field of view of the SEM. However, the results of the surface map are graphical rather than quantitative. The electron beam scans across the SEM field of view in a horizontal line, monitoring specific Auger transitions throughout the scan. As in the line scan analysis, resolution may be set at a maximum of 512 pixels per line. As the electron beam detects regions in which a high concentration of a particular element exists, these regions are assigned bright pixels. Likewise, areas of low elemental concentration are assigned dark pixels. Upon completion of the scan, the procedure repeats for the next immediate line. A maximum number of 512

lines may be acquired during a surface map analysis. At a resolution of 512 pixels per line, this analysis subdivides the SEM field of view into a two dimensional array of 512 x 512 pixels. The result is a detailed two-dimensional elemental distribution along the sample surface visible by the SEM. By way of example, figure 3.5 is a secondary electron micrograph of the surface of a research stage device precursor. Light and dark contrast areas are observed. Figure 3.6 is an Auger surface map of Sb in the field of view of the SEM image. It is clear that the regions of dark contrast are Sb rich relative to regions of light contrast. This Sb agglomeration is probably due to a phase segregation phenomenon as a result of high temperature annealing. At any rate, surface mapping provides two dimensional elemental distributions along the sample surface. From this work, a detailed chemical map of the beveled crater sidewall may be obtained. Different layers which are indistinguishable by SEM are clearly resolved by the Auger chemical map. Since chemical data corresponds to the SEM field of view, results of the Auger surface map conclusively identify the

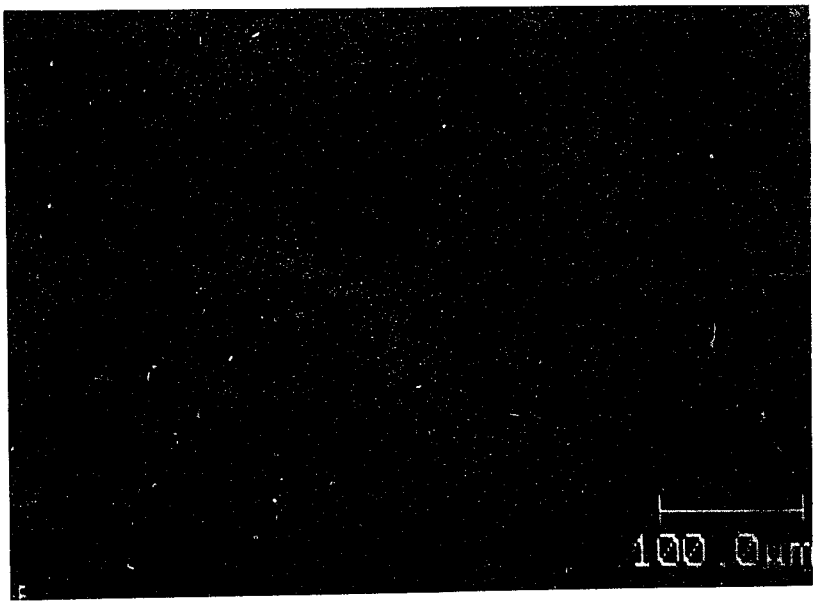

Figure 3.5 SEM image of research device prototype

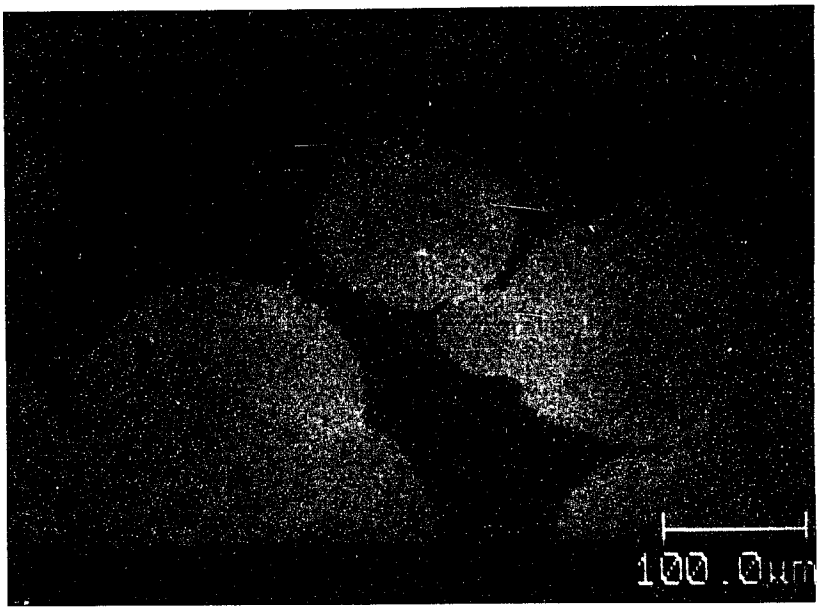

Figure 3.6 Auger surface map of Sb within SEM field of view

distinct layers on the SEM image which are previously unknown. In short, the Auger surface map data acquisition provides a vivid two dimensional graphical representation of the beveled crater sidewalls and is an available means of layer identification in instances where SEM cannot distinguish individual layers.

Another approach to resolving and measuring beveled layer thickness is required for electrically insulating samples. Characterization techniques in which an electron beam is incident upon a material require the material to be conductive. The impinging electron beam causes electrical charge to accumulate within the sample. In conductive materials such as metals and doped semiconductors, electronic charge transport mechanisms allow accumulated charge to dissipate at an appreciable rate. Namely, the dissipation rate should be equivalent to the rate at which electrical charge is incident onto the sample (i.e. primary electron current). Thus a steady-state condition is achieved in which the analyzed area effectively remains electrically neutral. SEM and Auger

analysis of such materials is straightforward. However, certain electrically insulating materials are characterized by extremely low conductivity [27]. This low conductivity prohibits the accumulated electrical charge of the electron beam from dissipating at the same rate at which charge enters the material. A steady-state condition is not achieved. The result is a net accumulation of electrical charge within the sample. This is known as sample charging [20]. With regard to chemical analysis, this excess charge causes shifting of Auger transitional energies, which in turn often affect measured peak intensities. In extreme cases, sample charging may significantly degrade peak shapes [28]. Auger data acquired under such a condition must be considered suspect, if not completely invalid. The Ar^+ ion beam may still be utilized to produce a crater with beveled sidewalls, but simultaneous Auger depth profiling or subsequent line scans or surface maps are generally of little use. Such techniques may not be employed to resolve distinct beveled layers for thickness measurements. With regard to structural analysis, sample charging also presents great difficulty in SEM characterization. Accumulated charge within the sample dynamically redistributes itself through Coulombic interaction. The secondary electron image is observed to move randomly about on the CRT monitor. Under these conditions, distinct beveled layers cannot be resolved by SEM. One solution to this problem is to deposit a thin (~100Å) gold film onto the sample surface. A Hummer VI sputtering system from Anatech LTD. is used for Au deposition. This is a commercial instrument used to plate surfaces with a conducting layer. Such a thin film provides a conductive path for incident electrical charge to dissipate, and SEM analysis may be performed. Another alternative for measuring layer thicknesses is analysis by optical microscopy. Incident light used as the probe in an optical microscope does not lead to the charging problems associated with an electron beam. Beveled layers may thus be resolved and measured using optical

microscopy, provided the indices of refraction of respective films are different. This method is particularly applicable to electrically insulating multi-layer structures in which adjacent layers are very similar in chemical composition. Despite the fact that Au deposition alleviates sample charging, the compositional similarity between adjacent films renders them difficult to distinguish by SEM. Hence beveled layers cannot be sufficiently resolved by SEM. In such cases, optical microscopy is a viable technique for measurement of beveled layer thicknesses.

3.2 Stylus Depth Profilometry

The bevel angle may be derived through stylus depth profilometry analysis. Measurements are performed using an Alpha-Step 300 depth profilometer from Tencor Instruments. This is a mechanical technique for measuring thickness differences between film steps. The instrument contains a stylus with a diamond tip 5 μm in diameter. The stylus comes in contact with the sample and is mechanically traced over a defined distance, recording vertical fluctuations in position as a function of lateral position. In this way, thickness differences between steps may be measured. While the lateral resolution of the instrument is determined by the tip diameter, there is greater sensitivity in the vertical dimension. Manufacturer specifications quote the vertical (depth) resolution to be approximately 10Å. This optimum resolution is not achieved due to environmental vibrational limitations [12]. Ambient noise has been measured at ± 80Å under typical operating conditions [29]. Despite the large noise level, vibration isolation tables may be employed to dampen vibrational and acoustic noise, decreasing the likelihood of introducing noise related artifacts into depth measurements. In addition, the instrument is fully computer automated and has multi-scan averaging capability. That is, a maximum number of ten profile scans

may be acquired over the same area and simultaneously averaged together. This averaging procedure serves to filter random vibrational noise, thus yielding depth measurements of suitable precision. Figure 3.7 is a typical example of a depth profilometry trace through a sputter crater produced by Auger depth profiling. The plot yields depth as a function of lateral scan position. Parameters of interest usually include the crater depth and smoothness of crater bottom and sidewalls. In this thesis, the sidewall characteristics are of interest. Measurements are performed on beveled sputter craters produced by prior Auger analyses of multi-layer structures. Through careful measurement, the beveled sidewall portion of the sputter crater may be identified. Once this is accomplished, the bevel angle is easily calculated by determining the slope of the stylus trace along the crater sidewall. The bevel angle and slope of the trace are related by a simple trigonometric function. Hence, by measuring the beveled layer thickness and calculating the bevel angle, actual film thicknesses may be derived.

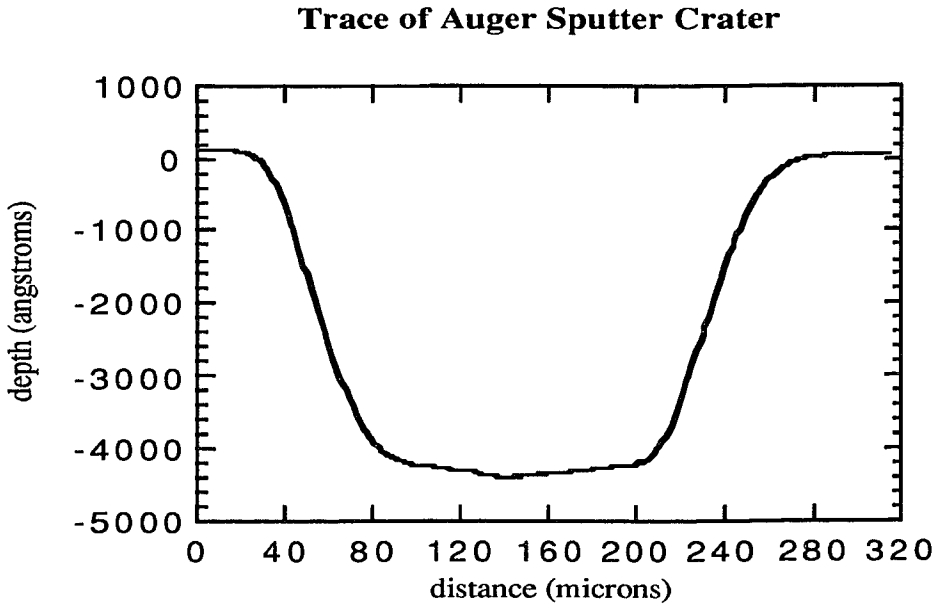

Figure 3.7 Depth profilometry scan of Auger sputter crater

3.3 Chemical Etching

For extremely thin layers, measurement of the beveled thickness by Auger line scanning becomes complicated due to the fact that the electron beam size becomes comparable to the thickness of the layer being probed. This is compounded by poor signal statistics acquired for very thin films, degrading the accuracy of the measurement. In these cases, device layers may be resolved by subjecting the beveled crater to a suitable chemical etch. This approach has been performed on alternating AlGaAs/GaAs superlattice layers in which the nominal thicknesses for the AlGaAs and GaAs layers are 200Å and 18Å respectively [30]. In addition, GaAs/InGaAs superlattice layers in which nominal GaAs layer thicknesses are 200Å and nominal InGaAs film thicknesses are 100Å have been chemically etched. For these layers, the wafer is etched in a 1:1 bleach (5% sodium hypochlorite) - DI water solution for five seconds, rinsed in DI water and blown dry with filtered nitrogen gas. This etch is preferential to GaAs [30]; that is, the GaAs layers chemically react with the etching solution and are eroded at a much greater rate than AlGaAs or InGaAs layers. This results in a step-like crater sidewall due to alternating GaAs layers being etched away and AlGaAs or InGaAs layers remaining relatively intact. Sidewall characteristics are readily observable by optical microscopy after etching. The etched sample is photographed using an optical microscope equipped with a green interference filter. In short, the chemical etching enhances sidewall features such that distinct layers are identifiable by optical microscopy at relatively low magnification. GaAs film thicknesses cannot be measured on post-etched samples because the layers of interest have been etched away. However, etching enables measurement of the remaining AlGaAs or InGaAs layers in the structure. Of equal importance is the qualitative uniformity information derived from this procedure. As was previously mentioned, typical

sputter craters comprise an area of 200 μm x 200 μm. Thickness fluctuations over such a large area may be visually inspected. This is true not only of AlGaAs layers, but any layer unaffected by the chosen chemical etch. In this way, the post-analysis chemical etch has great utility in monitoring semiconductor film growth processing.

CHAPTER 4

RESULTS AND DISCUSSION

4.1 Semiconductors

4.1.1 AlGaAs/GaAs Multiple Quantum Wells

Auger analysis is performed on an AlGaAs/GaAs multiple quantum well (MQW) structure developed for optical waveguide applications [31]. The device structure nominally consists of a period of 1400Å of $Al_{0.3}Ga_{0.7}As$ followed by 80Å of GaAs, repeated for 30 periods. This is followed by a 1.5 μm thick $Al_{0.3}Ga_{0.7}As$ layer, and subsequently the GaAs substrate. Figure 4.1 is an Auger intensity depth profile through the MQW. The various quantum well layers are clearly evident. As the Al Auger signal decreases, the Ga signal increases, corresponding to sputtering from an AlGaAs layer into a GaAs layer. The arrows on the right side of the plot indicate the dynamic range of

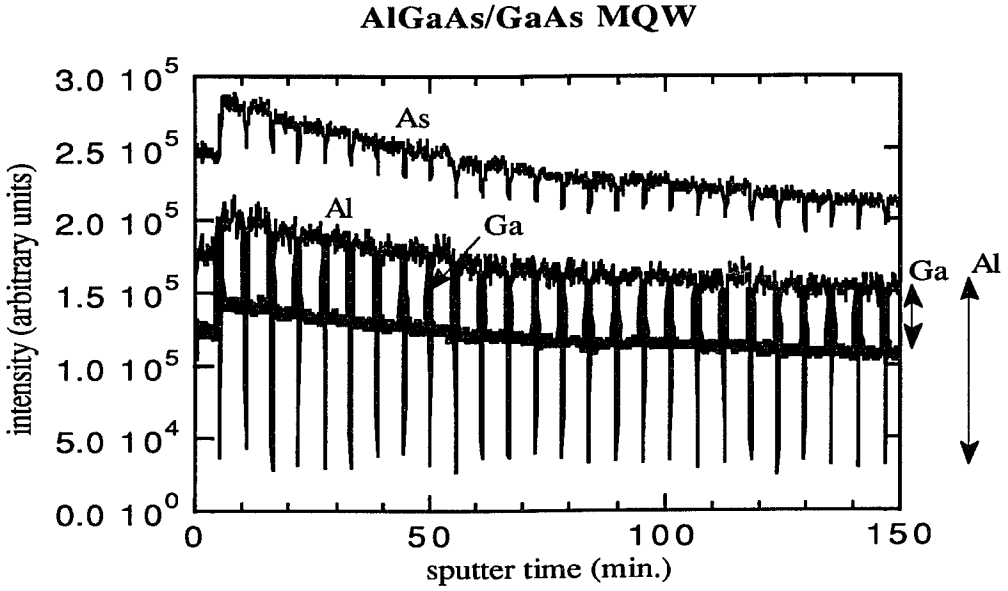

Figure 4.1 Auger intensity depth profile of AlGaAs/GaAs MQW

the Ga and Al signals respectively. Oscillations in the As signal are due to differences in Auger electron yield between GaAs and AlGaAs. At the end of the analysis, a sputter crater remains which is approximately 5 μm in depth. Figure 4.2 is an SEM micrograph of the resultant crater. Close observation reveals alternating light and dark contrast bands along the crater sidewall, most apparent near the top and bottom of the sidewalls.

The respective AlGaAs and GaAs layers within the MQW structure are revealed along the crater sidewall. In addition, the layers appear to be magnified to a considerable degree. Assuming nominal thicknesses, a 1400Å AlGaAs layer is clearly visible at low magnification along the crater sidewall. It appears that the sidewalls are beveled at an extremely shallow angle. In order to chemically identify respective layers, Auger surface map analysis is performed on the sputter crater . The Al Auger signal is monitored in the subsequent analysis. Figure 4.3 is a micrograph of the mapping results. Bright and dark regions indicate areas of high and low Al concentration respectively. Comparison with figure 4.2 reveals

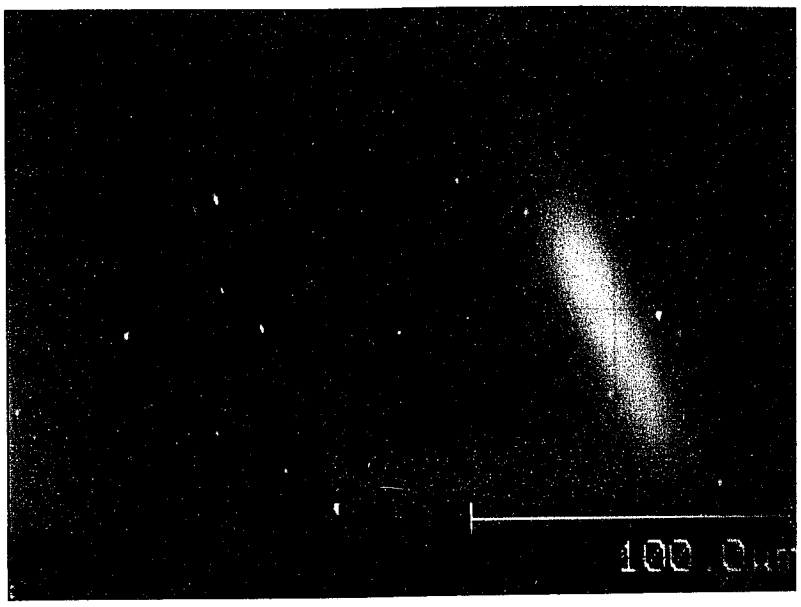

Figure 4.2 SEM micrograph of sputter crater of AlGaAs/GaAs MQW

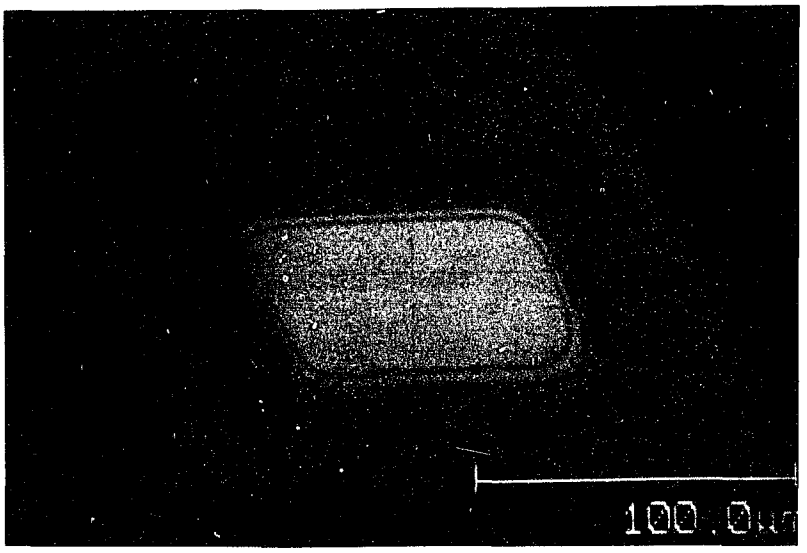

Figure 4.3 Micrograph of Al Auger surface map of sputter crater

that light contrast bands are Al deficient and dark contrast bands are Al rich. These correspond to GaAs and AlGaAs layers respectively. The bright region at the crater center in figure 4.3 is rich in Al, consistent with the fact that the MQW structure is grown on an AlGaAs layer. Thus, the central region is also AlGaAs. Through Auger surface map analysis, two dimensional chemical identification within the sputter crater has been accomplished.

Results of Al surface mapping of the MQW structure reveal device layer oscillations along the crater sidewalls. However, layer delineation over the central portion of the sidewall is impossible. Beveled layers are not thick enough to be properly resolved at low magnification, and as a result appear to be continuous over the center of the sidewall. A more detailed analysis of the MQW structure is warranted. The approach undertaken is to sputter through a smaller portion of the MQW and attempt to image and analyze a few AlGaAs/GaAs periods. Sputter craters are generated while continuously monitoring the Auger Al signal in order to determine the depth of the crater,

assuming nominal layer thicknesses. Ar^+ ion beam bombardment is terminated after sputtering through 5, 10, and 15 quantum well periods. Al Auger surface mapping is then repeated on each crater. Figures 4.4, 4.5, and 4.6 are micrographs of Al surface map results for craters sputtered through 5, 10, and 15 periods respectively. In figure 4.4, the five AlGaAs/GaAs periods are clearly visible. It is interesting that alternating layers appear to be much thicker in this figure than in figure 4.3, the analysis crater of the entire MQW structure, as both photographs are acquired at identical magnification. All layers are easily resolved in the present micrograph. Figure 4.5 shows that for 10 periods, distinct layers are resolvable, but the apparent thickness of each layer is decreased from the previous figure. For 15 quantum well periods in figure 4.6, each AlGaAs/GaAs layer is still resolved, albeit with increasing difficulty. Layers which appear to have a certain thickness in previous figures appear to be much thinner in the present figure. It appears that beveled layer thickness decreases with increasing sputter depth. Despite the fact that the bevel angle has yet to be

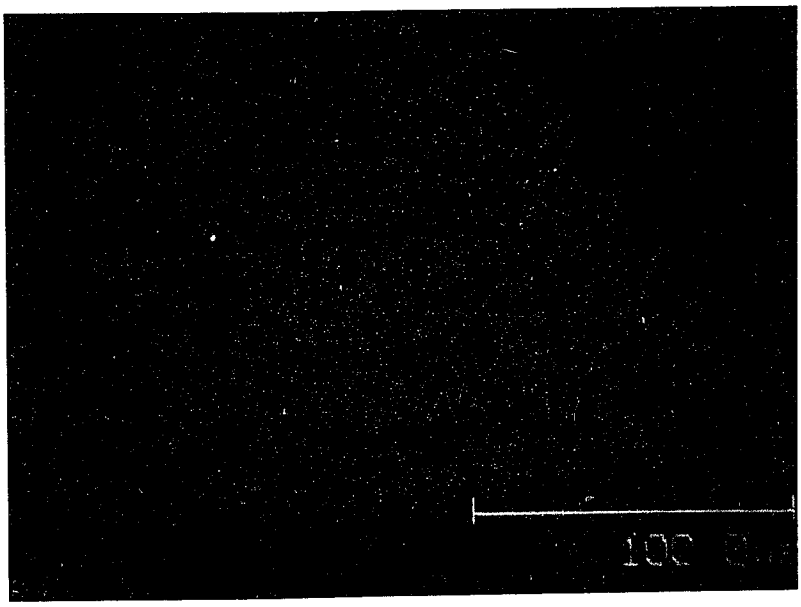

Figure 4.4 Micrograph of Al surface map through 5 MQW periods

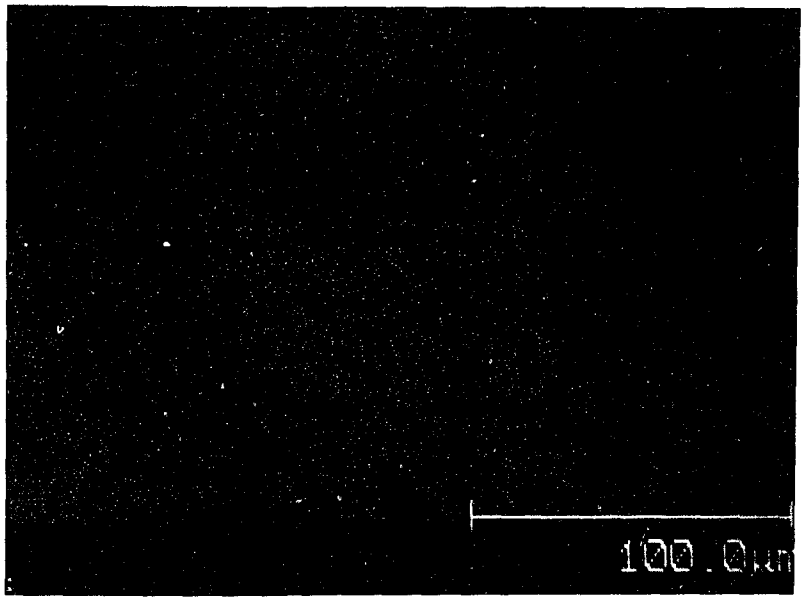

Figure 4.5 Micrograph of Al surface map through 10 MQW periods

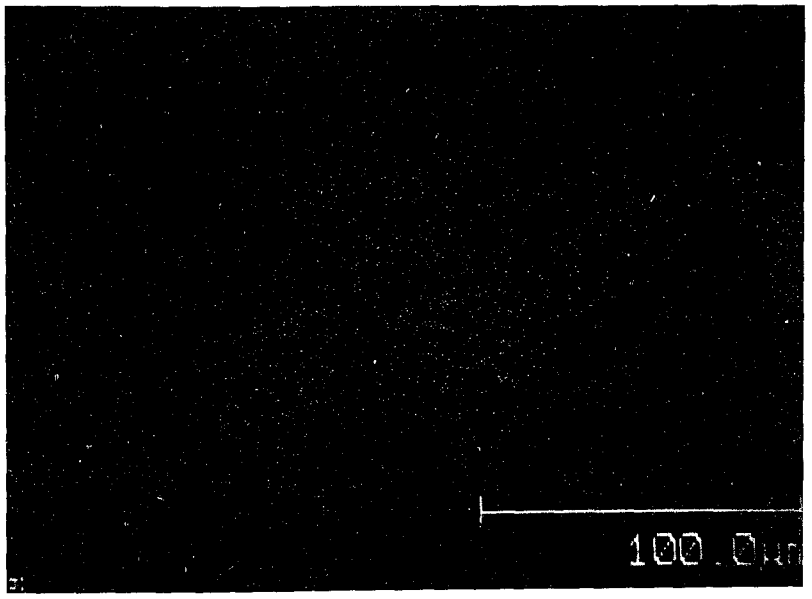

Figure 4.6 Micrograph of Al surface map through 15 MQW periods

measured, it is established that the angle is dependent upon depth of the sputter crater. Figures 4.4, 4.5, and 4.6 display the great utility of Auger surface mapping for qualitatively inspecting lateral uniformity of deposited layers. Spatial thickness variations are easily detected through such analysis. As figure 3.6 of the previous chapter displays, surface mapping also enables probing of elemental alloying or phase segregation along the surface of a sample. Auger mapping is a powerful technique for obtaining two dimensional chemical information associated with a secondary electron image.

The occurrence of shallow angle beveling by an ion beam may be explained through physical considerations. In theory, a plot of ion beam intensity as a function of position should yield a symmetrical Gaussian distribution [20]. Under optimum focusing conditions, the beam profile of the Ar^+ ion beam used to sputter etch materials should be reasonably close to a Gaussian curve. Figure 4.7 is an idealized Gaussian plot, depicting the theoretical shape of the Ar^+ ion beam. The beam intensity is highest at the center and decreases as $\exp(-x^2)$, the characteristic normalized Gaussian relation. As the Ar^+ beam is rastered during analysis, sputtering occurs from all portions of the beam. At the crater sidewalls, material is sputtered only by the outer tail of the ion beam profile. The central portion of the Gaussian beam never quite reaches these outer points. This area is sputtered at a slower rate than the center

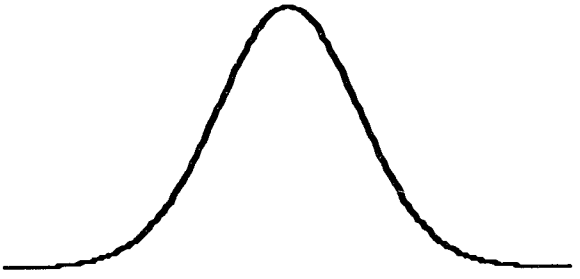

Figure 4.7 Theoretical Ar^+ ion beam profile

of the crater because of decreased ion beam intensity. At the most extreme crater edges, ion beam intensity is decreased further and material is sputtered at a correspondingly slower rate. Like the beam intensity, the sputter rate continuously decreases from the center of the beam to the outer portions of the Gaussian curve. It is due to this gradient in beam intensity that the material is differentially sputtered along the crater sidewalls, resulting in an effective bevel of the device structure being analyzed. If the beam is somewhat defocused, the beveling may further extend laterally and be even more pronounced than in an ideal case, yielding a subsequently more shallow bevel angle. With this model, it is reasonable to assume that the bevel angle will not be constant along the entire crater sidewall. Because of the gradual increase in intensity from the outer to inner portions of the beam, it is intuitively expected that the bevel angle will be very shallow at the outer portions of the crater sidewall. As the sidewall is traversed, it is expected that the bevel angle should increase. After this rise, whether the bevel angle remains constant on the crater sidewall is yet to be determined.

4.1.2 GaAs/InGaAs Multiple Quantum Wells

Another system extensively studied is a GaAs/InGaAs MQW structure. The sample is nominally comprised of 200Å of GaAs and 100Å of $In_{0.11}Ga_{0.89}As$, repeated four times. These four periods are grown on a GaAs substrate. This quantum well structure is used to study electronic transport phenomena in pseudomorphic high electron mobility transistors (p-HEMTs) [16]. Figure 4.8 is an Auger intensity depth profile of the device structure. Alternating GaAs and InGaAs layers are clearly observed. Oscillations in the Ga Auger signal are detected, although not nearly as pronounced at those of the In signal. This is due to a greater difference in In content than Ga content in successive layers.

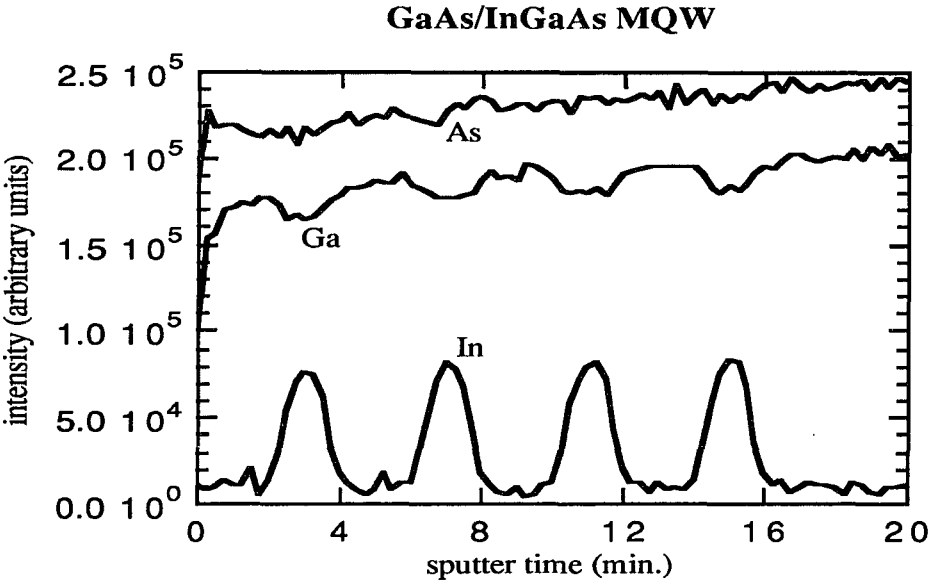

Figure 4.8 Auger depth profile of GaAs/InGaAs MQW

The In signal reflects layers which contain 5.5% at. In concentration and no In respectively. The Ga signal reflects layers containing nearly 45% at. Ga concentration and 50% at. Ga. Considering the percentages from peak to baseline for both signals, 5.5% at. In, in the presence of a baseline due solely to signal noise, is more readily detected than 50% at. Ga imposed on a 45% at. Ga concentration baseline. Due to this difference in percentage content, the In signal fluctuates with a higher dynamic range than the corresponding Ga signal.

After completion of the analysis, the sidewalls of the resulting sputter crater are observed to be beveled. Figure 4.9 is an SEM micrograph of the entire sputter crater. Close observation reveals the light contrast bands on the crater sidewalls amidst surrounding dark contrast material. These light bands are the InGaAs layers. Despite the fact that the depth profile detects four InGaAs layers, only three are resolved in figure 4.9. The MQW structure needs to be examined more closely.

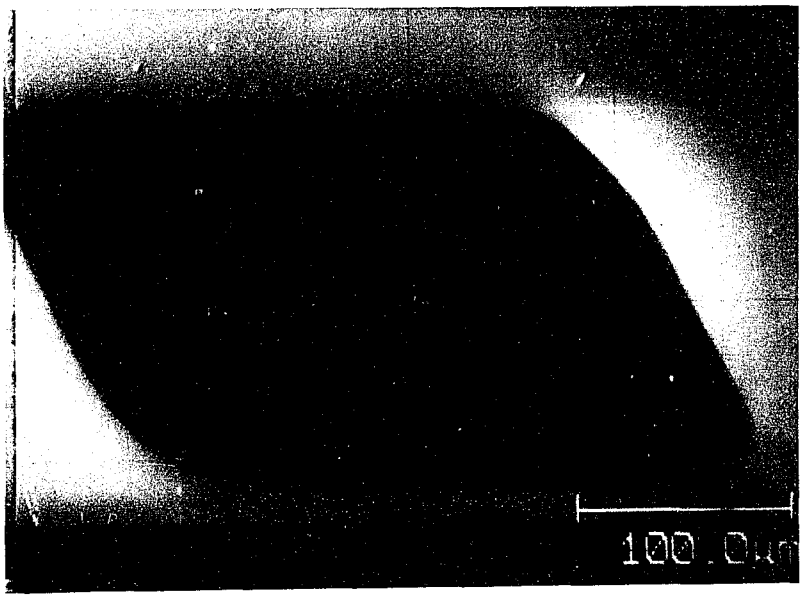

Figure 4.9 SEM image of GaAs/InGaAs MQW sputter crater

In order to measure the apparent beveled thickness of InGaAs layers, the Auger line scan technique is employed. The electron beam is scanned across the crater sidewall, continuously monitoring for the presence of In. Figure 4.10 is the resulting line scan for In. Signal intensity is plotted as a function of scan distance along the beveled sidewall. The four InGaAs layers in the MQW structure are revealed. Since the abscissa is in units of length, the apparent thickness of each InGaAs layer may be readily extracted from the plot. It is noted that the analysis is performed with the electron beam incident at an angle of 30° with respect to the surface normal. The reason for this is twofold. In the first place, Auger depth profile analysis is nearly always performed at this angle of incidence of the electron beam [23]. If the sample is tilted back such that the electron beam is incident normal to the surface, the energy spectrometer must be refocused. In short, performing the line scan analysis under the same conditions

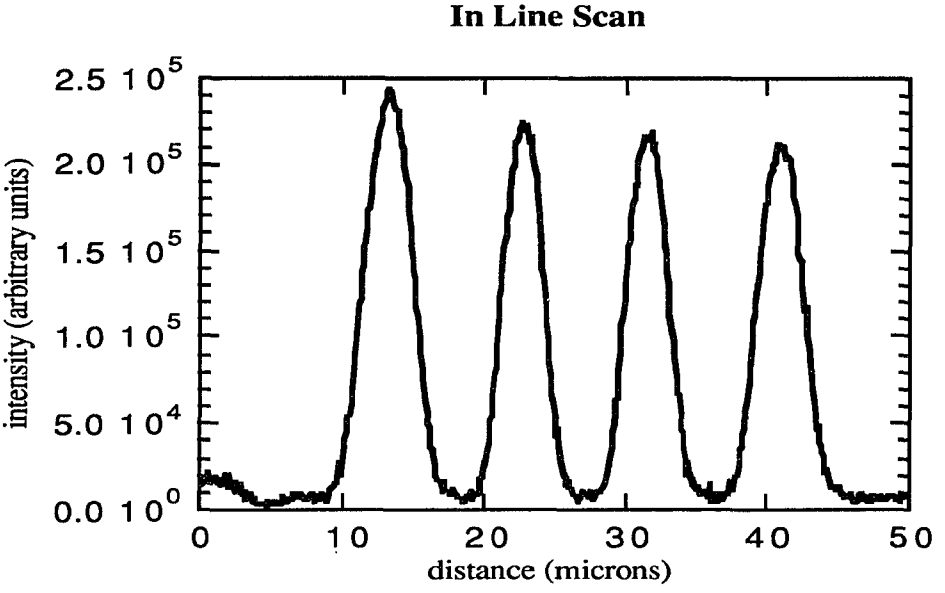

Figure 4.10 In Auger line scan across beveled MQW

as the depth profile analysis simply saves time. In addition, image contrast is enhanced when the sample is tilted due to the fact that the secondary electron detector on the system is not normal to the untilted sample, but at an angle of approximately 60° from the sample normal. If the sample is tilted towards the detector, the sharpness and contrast of the image improves. Therefore, line scanning is performed at the same angle as depth profiling, namely at an electron beam incidence of 30° from surface normal. However, this angular parameter must be accounted for in measuring beveled layer thicknesses. At an arbitrary sample tilt, the electron beam images or measures a projection of the actual layer thickness. Figure 4.11 illustrates the geometric representation of a sample tilted by angle ß. The value of interest is the layer thickness at the surface. However, the incident electron beam sees the projection h to be the layer thickness. The actual beveled thickness is h/cosß from elementary geometry. Hence, layer thicknesses measured from the line scan plot acquired at a tilt angle of 30° must

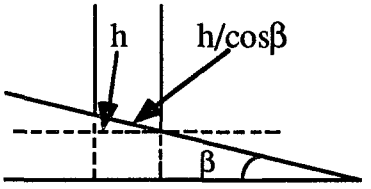

Figure 4.11 Geometric schematic for measuring layer thicknesses

be divided by a factor of cos 30° in order to obtain true beveled thicknesses.

With Auger depth profiling and line scanning complete, imaging of the MQW structure is in order. Figure 4.12 is an SEM image of the beveled crater sidewall. The In line scan observed in figure 4.10 is superimposed vertically upon the image as an aid in resolving distinct layers. Although difficult to detect, the image contains four horizontal bands characterized by lighter contrast than the surrounding material. These are the InGaAs MQW layers. The darker bands surrounding the InGaAs bands are the GaAs layers. By focusing on the superimposed In line scan, the beveled InGaAs layers may be observed.

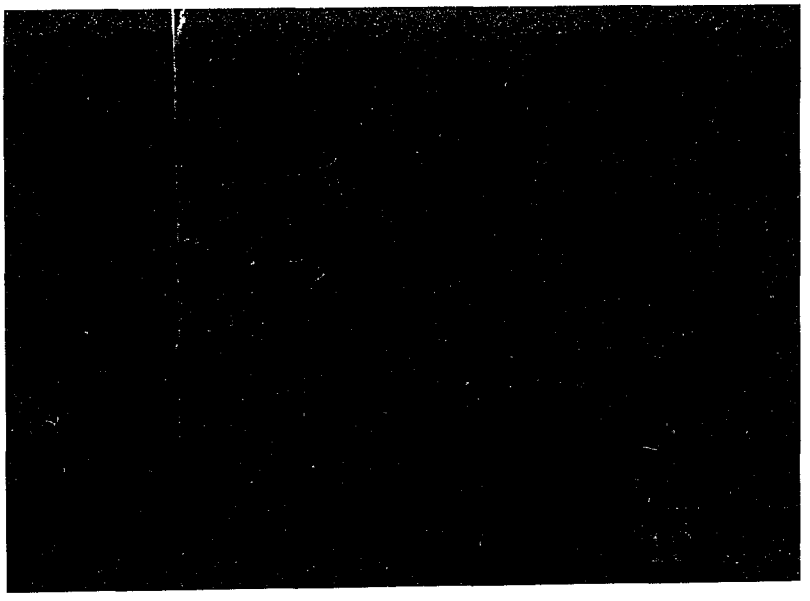

Figure 4.12 SEM image of sidewall of GaAs/InGaAs MQW

A question arises as to where an InGaAs layer begins and ends in figure 4.10. A simple model of the scanning electron beam is developed in order to answer this question. At the heart of this model is the theoretical assumption that the electron beam intensity profile is a three dimensional Gaussian volume. This being the case, half of the electron beam intensity is contained within exactly half of this volume [32]. In considering InGaAs layers in figure 4.10, the point at which the In signal rises to half the maximum value corresponds to the electron beam being positioned such that exactly half of the beam is over the InGaAs film. At this point, half of the beam intensity contributes to In Auger transition generation. Figure 4.13 is a graphical schematic of a scanning electron beam of diameter d progressing through a film of beveled thickness h. The electron beam moves from left to right, and the Gaussian character and size of the beam is grossly exaggerated. At position a), half of the electron beam is outside the beveled layer and half of the beam intensity contributes to Auger electron generation; thus the In signal in figure 4.10 rises to half of its maximum value. At position b), the entire electron beam volume is contained within the InGaAs film. At this point, the entire beam is contributing to In Auger transitions; thus the In signal in figure 4.10 rises to full intensity. At position c), the beam is exiting the InGaAs film and is at the point in which exactly half of the beam intensity contributes to In Auger electron generation; thus, the In signal in figure 4.10 again decreases to half the maximum value. In the course of this progression, the electron beam has traveled a distance h, the beveled layer thickness. Therefore, with this model, an electron beam scanning through a beveled film and monitoring Auger transitions through line scanning data acquisition shall traverse the beveled thickness of the film between the two full width-half maximum intensity points of the elemental line scan plot. Thus beveled layer thicknesses may be directly measured from the line scan

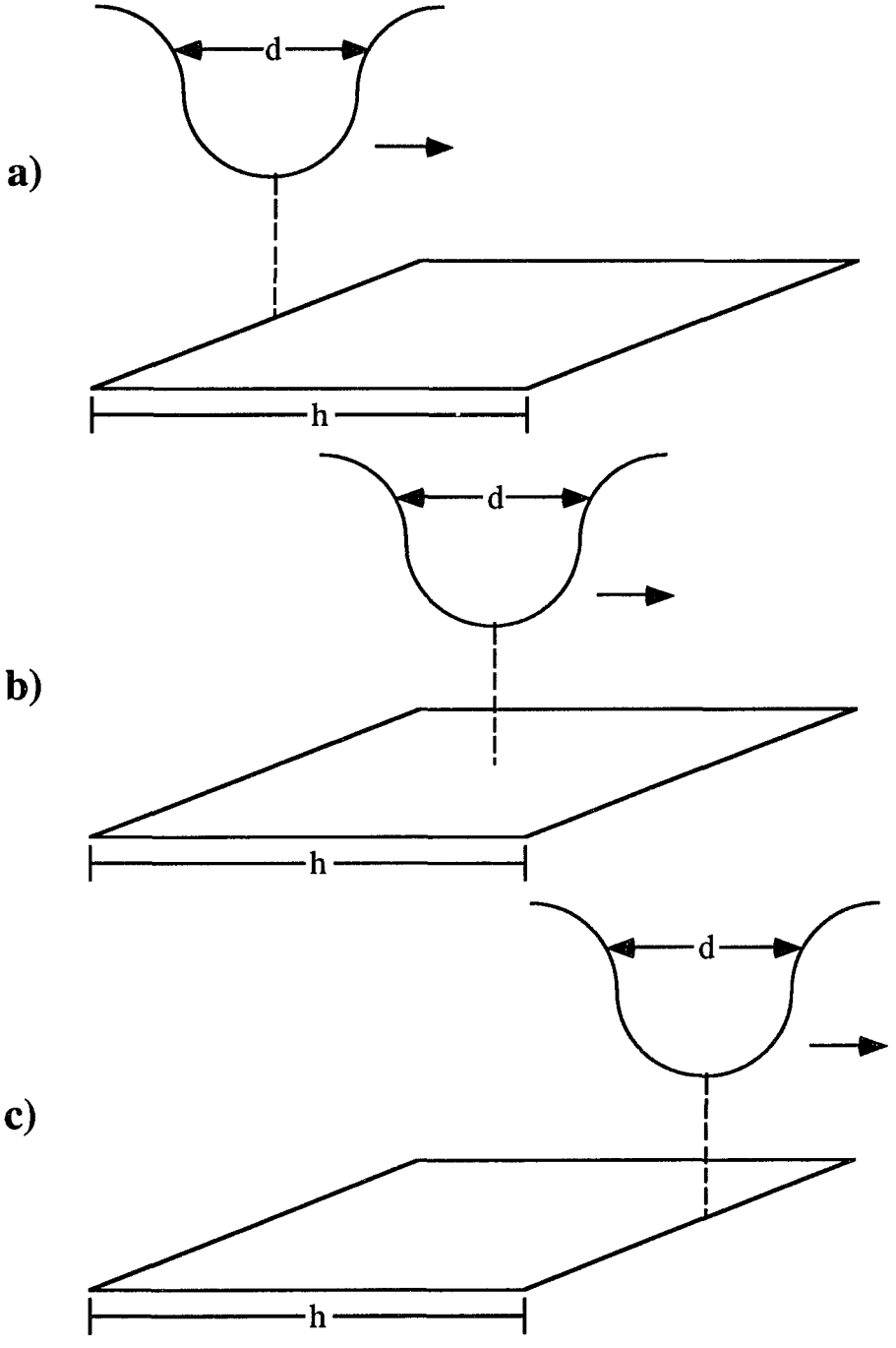

Figure 4.13 Schematic of scanning electron beam progression

intensity plot, without accounting for the finite size of the scanning electron beam. An inherent assumption in this formulation is that the electron beam is smaller in diameter than the thickness of the beveled film being probed. If the beam is found to be larger than the beveled film, then the correspondence between the full width-half maximum intensity points and physical location of the scanning electron beam is no longer valid. Thus, in order for the model to hold, experimental parameters during Auger line scanning must be such that the electron beam is smaller in diameter than the beveled device layers being measured. This will be verified through electron beam size measurements.

According to the above model, beveled thicknesses may simply be extracted from Auger line scanning results. The next step is a precise bevel angle measurement through stylus depth profilometry. Figure 4.14 illustrates the results of depth profilometry measurements along the beveled crater sidewall. The abscissa is lateral trace distance and the ordinate is crater depth along the sidewall. Crater depths are assigned negative values. To understand how the

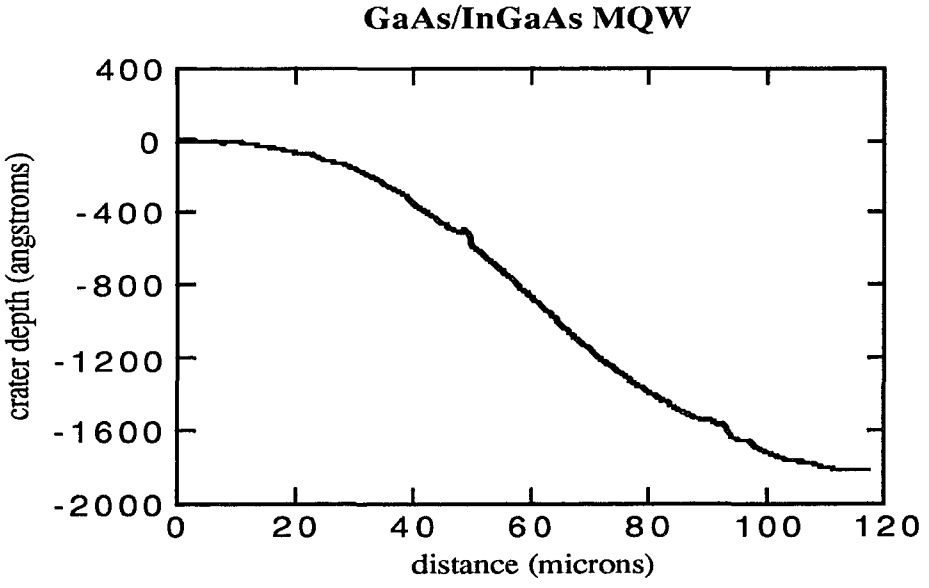

Figure 4.14 Depth profilometry trace along MQW sidewall

bevel angle is derived from the plot, the relationship between film thickness d, scan distance h, and bevel angle α is depicted in figure 4.15. From this figure, the following relationship holds:

$$\tan \alpha = d/h$$

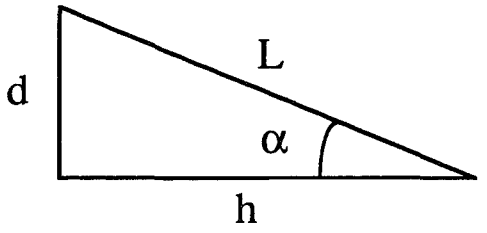

Figure 4.15 *Schematic relating bevel parameters to film thickness*

From a comparison of figure 4.15 with the depth profilometry trace of figure 4.14, it is clear that the scan distance h is plotted on the abscissa, film thickness d is plotted on the ordinate, and bevel angle α is related to the slope of the trace M by the following simple equation:

$$\tan \alpha = M$$

Hence, by simply determining the slope of the profilometry trace, the bevel angle α is obtained. Inspection of figure 4.14 immediately shows that the bevel angle is not constant but continuously varies along the beveled crater sidewall. Since lateral position and crater depth at each point along the profilometry trace are known, the bevel angle for any segment along the sidewall may be directly determined by calculating the slope of the trace. In order to probe the variation in bevel angle with crater depth, the ordinate of figure 4.14 is divided into 100Å segments. For each segment, the lateral distance which the crater depth

subtends by a 100Å decrease is measured. Dividing the change in crater depth by the change in lateral position yields the slope of the segment. By using the above relation tan α = M, the bevel angle is calculated. For example, a decrease from the sample surface to a crater depth of 98Å results in a change in lateral position of 26.1 μm. The slope of this segment is:

$$M = 0.0098\ \mu m / 26.1\ \mu m = 0.00038$$

From the above relation:

$$\tan \alpha = M = 0.00038 \dashrightarrow \alpha = 0.022°$$

This procedure is repeated for successive 100Å segments. The results are illustrated in figure 4.16. Each angle determined is plotted at the midpoint of the segment used in the calculation. The bevel angle determined from the crater

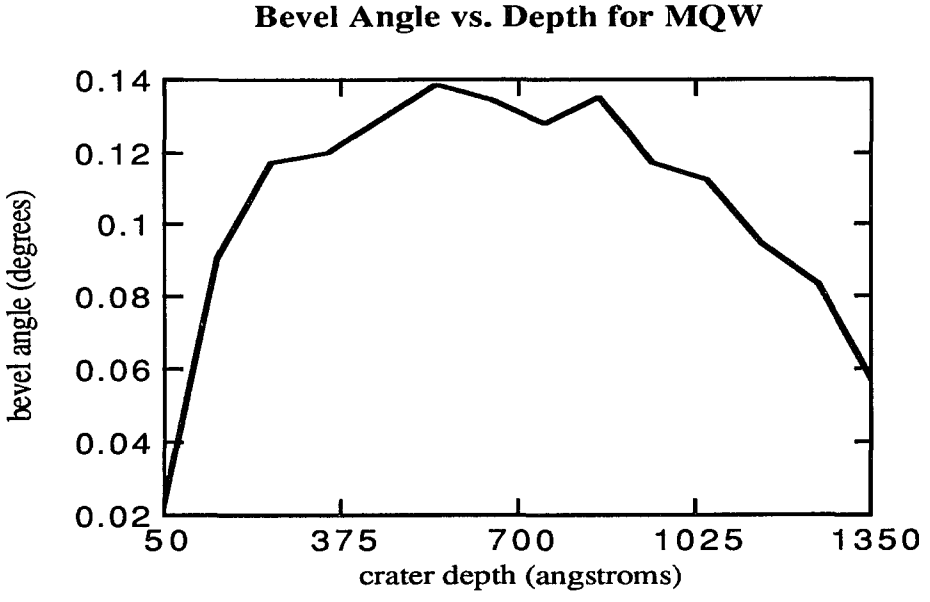

Figure 4.16 Variation of bevel angle with depth along sidewall

depth segment 400Å-500Å is plotted at a crater depth of 450Å. In short, the plot behaves as previously described. The angle is very shallow at the top of the sidewall, which is consistent with the explanation that the beveling phenomenon is a result of differential sputtering along the sidewall by the tail of the Gaussian Ar^+ ion beam. The angle increases and remains relatively constant throughout the central portion of the crater sidewall. The angle then decreases once again as the crater bottom is approached. The sidewall regions near the sample surface and crater bottom are not useful for determining film thicknesses due to sharp variations in the measured bevel angle. Furthermore, the sidewall region near the sample surface is susceptible to sample material pile-up induced by ion beam sputtering, altering the measured bevel angle. Thus, these regions shall be avoided in calculating film thicknesses. Despite this, the central portion of the sidewall is characterized by an approximately constant bevel angle. Thicknesses of device layers which lie in this region of the beveled sidewall may be measured.

Since the beveled length of GaAs and InGaAs layers have now been measured and the bevel angle determined, film thicknesses may be calculated from figure 4.15:

$$d = L \sin \alpha$$

The bevel angle is calculated over the central portion of the sidewall region in which the angle is relatively constant. Over this region, the bevel angle is determined as follows:

$\tan \alpha = M = (0.1365\ \mu m - 0.0762\ \mu m) / (89.92\ \mu m - 67.58\ \mu m) \rightarrow \alpha = 0.16°$

Due to the bevel angle variation near the top of the crater sidewall, no thickness values are calculated for the first GaAs/InGaAs period and the second GaAs layer. Calculations are performed for the next InGaAs layer and subsequent two GaAs/InGaAs quantum well periods. Thickness values are compared to results from transmission electron microscopy (TEM) measurements. GaAs and InGaAs layer thicknesses as measured by TEM are 200Å and 108Å respectively. The accuracy of TEM measurements is ±2Å [33]. The results are summarized in Table 4.1. Thickness measurements of the InGaAs layers are in excellent agreement with TEM results. Beveled lengths for GaAs layers are taken as the differences between successive InGaAs layers. Ga line scans across the beveled crater sidewall have been acquired, but are not used in thickness calculations due to inconclusive layer delineation caused by poor signal statistics. The fact that GaAs layer thicknesses are derived indirectly through InGaAs measurements may cause the inaccuracy observed in GaAs thickness calculations relative to that of InGaAs. In short, thickness measurements derived by the shallow angle beveling technique compare favorably with those measured by TEM analysis.

Table 4.1 Beveling Parameter Values for GaAs/InGaAs MQW

Layer	Bevel Length L (μm)	Bevel Angle α (degrees)	Thickness d=L sinα (Å)	TEM Results (Å)
InGaAs	3.80	0.16	103	108
GaAs	6.33	0.16	172	200
InGaAs	3.91	0.16	106	108
GaAs	6.79	0.16	184	200
InGaAs	4.14	0.16	112	108

4.1.2.1 Error Analysis

With InGaAs and GaAs layer thicknesses calculated, the accuracy of these measurements needs to be addressed. Film thicknesses are the product of beveled layer thickness with the sine of the bevel angle. Auger line scan

analysis and stylus depth profilometry are used to measure each of these quantities. Therefore, accuracy of film thickness is determined by the error bars associated with both of these measurements.

To probe the accuracy of Auger line scanning, an SEM standard, certified by the National Institute of Standards and Technology (NIST), is analyzed under identical conditions as the GaAs/InGaAs MQW structure. The standard consists of linear and rectangular features in which the size of each feature is very well known. The standard is composed of an 800Å Cr surface layer deposited on a thin layer of indium tin oxide (ITO), an electrically conductive glass. This in turn is mounted on a fused silica substrate. Auger line scans of Cr are acquired over a variety of rectangular features. The results of the analyses are summarized in table 4.2. Measured thicknesses by Auger line scanning are observed to agree very well with certified nominal thicknesses. Calculating the root-mean-square deviation of the absolute error values, which is statistically defined as the standard deviation σ of the measurements [34], this value is determined to be σ=0.14 μm. In this way, the error associated with Auger line scan measurements is determined to be 0.14 μm. Since the thinnest InGaAs film measured is approximately 3.8 μm, the error in the measurement is less than 5% and is thus acceptable.

Table 4.2 Accuracy Measurement of Auger Line Scanning

Nominal Thickness (μm)	Measured Thickness (μm)	Absolute Difference (μm)	Percent Difference (%)
2.6	2.53	0.07	2.87
2.8	2.64	0.16	5.71
3.0	2.81	0.19	6.25
3.2	3.01	0.19	5.83
4.6	4.48	0.12	2.68
4.8	4.71	0.09	1.95
5.0	4.88	0.12	2.43

Accuracy assessment of depth profilometry measurements is estimated through the same methodology. A VLSI depth profilometry standard is employed. The section analyzed consists of a periodic series of SiO_2 steps on a Si die. The step periodicity is known to be exactly 10 μm and the depth is certified to be 4463Å. A trace over 12 step periods is acquired. Results of the analysis is illustrated in table 4.3. Period distance is not measured for the first step because periodic measurements require a reference point, and there is no such reference point for the initial measurement. Excellent accuracy in depth measurements is obtained. The accuracy of lateral scan measurements is within ±5% of the nominal value, with the exception of one spurious data point. Calculated standard deviation of depth and lateral measurements are 7Å and 0.54 μm respectively. The data indicate that stylus depth profilometry is accurate in both horizontal and vertical directions. Since the bevel angle is derived from a quotient of vertical and horizontal measurements, the bevel angle should be reasonably accurate.

Table 4.3 Accuracy Measurement of Stylus Depth Profilometry

Depth (Å)	Absolute Difference (Å)	Percent Difference (%)	Period Distance (μm)	Absolute Difference (μm)	Percent Difference (%)
4463	0	0	N/A *	N/A *	N/A *
4453	10	0.22	9.87	0.13	1.3
4468	5	0.11	9.57	0.43	4.3
4462	1	0.02	10.17	0.17	1.7
4448	15	0.34	9.57	0.43	4.3
4462	1	0.02	9.57	0.43	4.3
4467	4	0.09	10.16	0.16	1.6
4461	2	0.04	10.47	0.47	4.7
4461	2	0.04	10.47	0.47	4.7
4464	1	0.02	10.46	0.46	4.6
4449	14	0.31	11.37	1.37	13.7
4457	6	0.13	10.16	0.16	1.6

* Not applicable

The accuracies calculated for line scan and depth profilometry measurements must be translated into accuracy in thickness measurements. Recall the relation between thickness d, beveled length L, and bevel angle α:

$$d = L \sin \alpha$$

From elementary calculus, the differential form of the chain rule for a continuous function of two variables F(x,y) states [35]:

$$dF = (\delta F/\delta x)\, dx + (\delta F/\delta y)\, dy$$

where $\delta F/\delta x$ and $\delta F/\delta y$ are partial derivatives of F with respect to x and y. Applying this equation to the previous expression $d = L \sin \alpha$:

$$\Delta d = (\delta d/\delta L)\, \Delta L + (\delta d/\delta(\sin \alpha))\, \Delta(\sin \alpha)$$

Substituting and differentiating:

$$\Delta d = \sin \alpha\, \Delta L + L\, \Delta(\sin \alpha)$$

The uncertainty in beveled length ΔL is the standard deviation of Auger line scan measurements previously calculated, 0.14 μm. The angular uncertainty $\Delta(\sin \alpha)$ depends on the horizontal and vertical uncertainties independently derived through depth profilometry measurements for the VLSI standard. From the previous data:

$$\Delta(\tan \alpha) = 7\text{Å}/5400\text{Å} \;\text{--}\!\!>\; \Delta(\tan \alpha) = 0.0013$$

For small angles, $\tan \alpha \approx \sin \alpha$ [35]. Therefore:

$$\Delta(\sin \alpha) \approx \Delta(\tan \alpha) \text{ --> } \Delta(\sin \alpha) = 0.0013$$

Since ΔL and $\Delta(\sin \alpha)$ are derived from the standard deviations determined from analysis of standards, they apply to all materials systems, as well as the GaAs/InGaAs MQW structure. Thus, the uncertainty in calculated thickness may be expressed as:

$$\Delta d = 0.14 \sin \alpha + 0.0013 \, L \quad (\text{in } \mu m)$$

or

$$\Delta d = 1400 \sin \alpha + 13 \, L \quad (\text{in } Å)$$

For each measurement, L and sin α are measured, and the uncertainty in thickness is given by this expression. The calculation is straightforward, and table 4.4 is actually table 4.1 incorporating calculated accuracies for each device layer. The error bars are approximately ±50% of the measured layer thickness. The accuracy of the measurement is not very good. To explain this, consider the first InGaAs layer. Substituting L and sin α into the previous expression:

$$\Delta d = 1400 \sin(0.16°) + 13 \, (3.80) \quad Å$$

Table 4.4 Beveling Parameter Values for GaAs/InGaAs MQW (revised)

Layer	Bevel Length L (μm)	Bevel Angle α (degrees)	Thickness d=L sinα (Å)	TEM Results (Å)
InGaAs	3.80	0.16	103 ± 53	108 ± 2
GaAs	6.33	0.16	172 ± 86	200 ± 2
InGaAs	3.91	0.16	106 ± 55	108 ± 2
GaAs	6.79	0.16	184 ± 92	200 ± 2
InGaAs	4.14	0.16	112 ± 58	108 ± 2

Simplifying:

$$\Delta d = 4 + 49 = 53\text{Å}$$

The associated uncertainty is dominated by the second term. The first error term in the calculation is due to uncertainty in L, the beveled layer thickness measured by Auger line scanning. The dominant error term is due to uncertainty in sin α, that is, the bevel angle determined from depth profilometry measurements. The source of uncertainty lies not in the precision of measurement, but in the subjective nature of defining the bevel angle. The bevel angle is defined by the slope of the depth profilometry trace along the central portion of the crater sidewall. The region is chosen visually from the trace. The endpoints defining the bevel angle are chosen to encompass the largest linear area possible, avoiding angle fluctuations or defects along the crater sidewall. This is a relatively imprecise method of defining the region of constant slope. Numerous endpoints defining the bevel angle may be chosen, each yielding a slightly different angle. A small change in the measured angle results in a large change in calculated layer thickness. In short, the imprecise nature of defining the bevel angle leads to relatively large uncertainty in calculated film thicknesses. Emphasis of future work will be placed on standardizing a systematic procedure for defining the bevel angle with increased precision. Despite the large uncertainty, thicknesses determined by the technique compare very well with those obtained using TEM.

The favorable nature of results lends credibility to assumptions regarding electron beams made in this work. However, the size of the electron beam remains to be verified. Recall from previous discussions that electron beam diameter need not be taken into account in measuring beveled layer thicknesses

so long as the beam is smaller than the layer being probed. In order to verify this assertion, electron beam size measurements are performed using a standard Au grid. The electron beam is scanned over the grid and beam diameter is measured by the rolloff of the beam from the Au grid to a vacant area. A reverse scan from a vacant area to the Au grid is equally valid. The results of the measurement are illustrated in figure 4.17. Intensity is plotted as a function of scan distance as the beam traverses the Au grid. The beam diameter is defined as the distance between the two points on the curve which are located at 20% and 80% of the maximum intensity. This method of measuring beam diameter inherently assumes that the electron beam profile is a Gaussian volume and the outer tail of the Gaussian curve is omitted [36]. By performing this procedure, the electron beam diameter is measured to be 5080Å for the given analytical conditions. In reviewing table 4.1, the beam size is smaller than the thinnest beveled layer probed. Hence the assumptions are self-consistent and calculated thicknesses are in agreement with thickness measurements acquired by TEM. Presently,

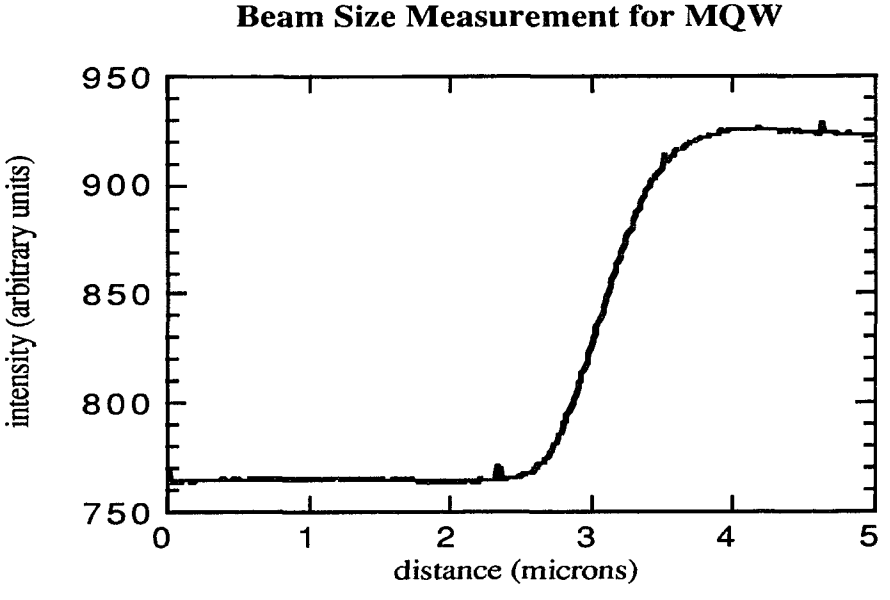

Figure 4.17 Electron beam diameter measurement

while the technique does not approach the time honored accuracy of TEM measurements [17], the procedure may be performed in under a day's time and is very simple. Thus, a trade-off exists between accuracy and ease of procedure.

4.1.3 Pseudomorphic High Electron Mobility Transistor

The technique is applied to a GaAs-based pseudomorphic high electron mobility transistor (p-HEMT) [30]. This is a microwave monolithic integrated circuit (MMIC) device designed to operate at high frequencies. Figure 4.18 is a design schematic of the nominal p-HEMT device . The most critical layer in the device structure is the $In_{0.22}Ga_{0.78}As$ film. This is the electrically active layer of interest in the device [10]. Si layers of thickness d are planar sheets of Si atoms. The two Si d-doped layers coupled with the InGaAs film perform the transistor

n+ GaAs cap	50Å
AlGaAs	350Å
Si plane	δ
AlGaAs	25Å
InGaAs	120Å
GaAs	30Å
AlGaAs	20Å
Si plane	δ
AlGaAs	180Å
GaAs(15Å)/AlGaAs(200Å) [X20]	
GaAs substrate	

Figure 4.18 Nominal device schematic of MMIC p-HEMT

action of the device. In addition, a GaAs(15Å)/AlGaAs(200Å) superlattice of 20 periods is incorporated into the device. The purpose of the superlattice is to provide a smooth surface on which to grow subsequent films [9].

Figure 4.19 is an Auger intensity depth profile of the p-HEMT. All elemental signals are clearly labeled. Each layer of the nominal design is observed, with the exception of the d-doped layers because the nominal Si dose is below the detection limits of the Auger technique. All periods of the GaAs/AlGaAs superlattice are resolved, as evidenced by the Al and Ga signal oscillations within the superlattice region. The profile interval from approximately t=10 minutes through t=15 minutes should be noted. This is the region between the AlGaAs layer immediately following the second Si d-doping and the GaAs/AlGaAs superlattice. This portion of the profile is characterized by baseline Al and In signals and a relatively high Ga signal. Absence of Al and In indicates that this layer consists of GaAs. Comparison with the design schematic in figure 4.18 shows that the GaAs layer is unintentional. Detection

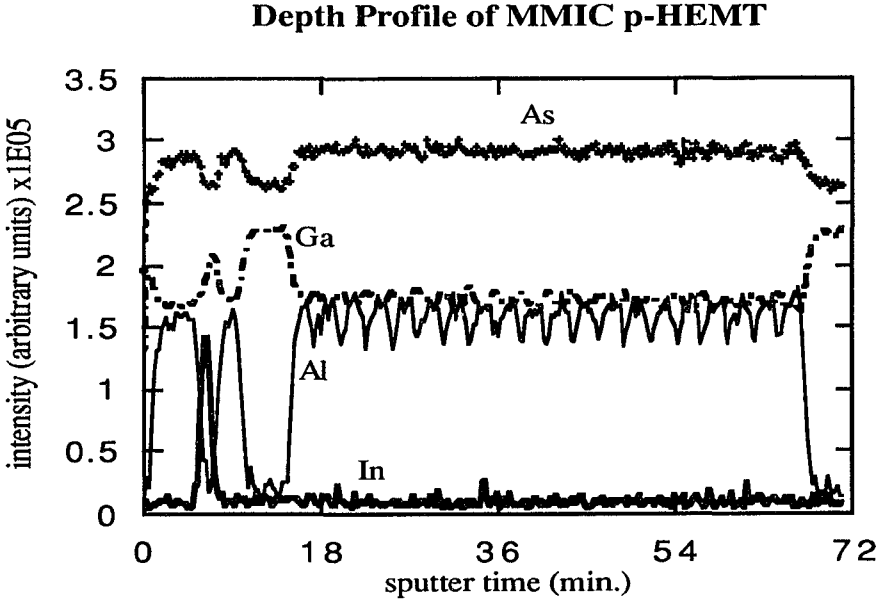

Figure 4.19 Auger intensity depth profile of MMIC p-HEMT

of this extra layer helps to explain unexpected electrical characteristics for the device. The sputter crater associated with the depth profile analysis is illustrated in an SEM image in figure 4.20. Layers of varying contrast are immediately noted. The following interpretation assumes nominal film thicknesses from the design schematic. The surface of the sample consists of GaAs, as there is a 50Å n^+ GaAs layer capping the device. Progressing down the crater sidewall, the first region of dark contrast is an AlGaAs layer. This layer consists of the 350Å AlGaAs film, the first Si d-doping, and the following 25Å AlGaAs film. Since the d-doped layer is not detectable by Auger spectroscopy, distinct AlGaAs films appear as one layer, both in the depth profile and on the SEM image. The next section features two bands of light contrast separated by a layer of dark contrast. The first light contrast section is a combination of the 120Å InGaAs layer and subsequent 30Å GaAs layer. Since both InGaAs and GaAs are characterized by light contrast on a secondary electron image, the different films appear as one. The next dark contrast band is comprised of the subsequent 20Å

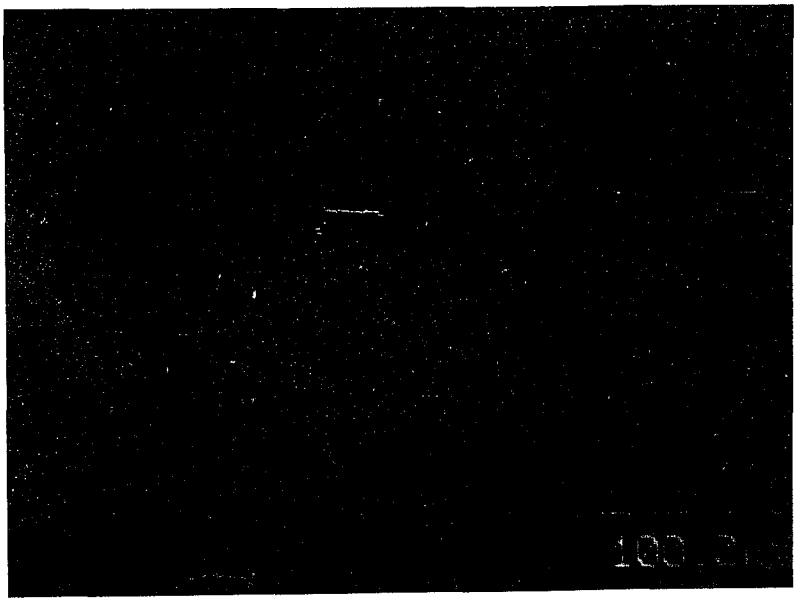

Figure 4.20 SEM image of p-HEMT beveled sputter crater

AlGaAs, second d-doping, and 180Å AlGaAs layers. The next band of light contrast is the extra GaAs layer which is detected in the Auger intensity depth profile. The thickness of this layer has yet to be determined. The broad dark contrast film is the GaAs/AlGaAs superlattice layer. Finally, the light contrast crater bottom is the GaAs substrate. Figure 4.20 is a striking visual representation of the results of the ion beam beveling phenomenon. Layers which are nominally 100-200Å thick are readily observed on an SEM image at low magnification. Since the sputter crater size is 200 μm x 200 μm, various layers are observed over a large area. This feature facilitates qualitative lateral uniformity studies of film growth processes.

The depth profilometry results for the GaAs/InGaAs MQW in the previous section show that the bevel angle varies continuously along the sputter crater sidewall. Thickness measurements of layers which lie on a sidewall region in which the bevel angle varies are not meaningful because thickness is the product of measured beveled length with sin α, where the bevel angle α is assumed to be constant. If device layers of interest lie on the sidewall portion in which α is constant or approximately so, then derived layer thicknesses are valid. In reviewing results of the previous section, it is apparent that the bevel angle is approximately constant within the central portion of the crater sidewall. Films which lie within this range on the sidewall may be properly measured. If it is possible to perform experiments in such a way that device films to be measured lie on this section of the sidewall, then all films may be measured at a constant bevel angle. Since the angular variability occurs near the top of the sidewall and towards the crater bottom, it is conceivable that deposition of a film onto the structure to be analyzed may be of value [26]. The purpose of this deposited film is to act as a sacrificial overlayer so that the bevel angle variation near the top of the sidewall occurs within this layer. This being the case, device layers

beneath the overlayer will fall within the sidewall region of constant bevel angle. In addition, since the bevel angle varies near the crater bottom, ion beam sputtering must be continued for some time after the layers of interest have been sputtered through in order to have the region of variable angle occur beneath layers to be measured. In effect, layers of interest are forced to lie within the central portion of the sidewall, the portion of constant bevel angle. After studying previous results, it is empirically determined that the region of variable bevel angle near the top of the crater sidewall comprises approximately 25% of the total sidewall. That is, one-fourth of the total crater depth at the top of the sidewall is characterized by a variable angle. Likewise, angle variations occur over one-fourth of the total crater depth near the crater bottom. Assuming the nominal p-HEMT design structure, relevant device layers comprise a total depth of 5075Å. Thus, a sacrificial layer of approximately 2500Å in thickness should be deposited on the p-HEMT device. Furthermore, after the GaAs/AlGaAs superlattice has been sputter etched, approximately 2500Å of GaAs substrate material should be sputtered through in order to confine bevel angle variability within the substrate material. Therefore, a Au overlayer is sputter coated onto the sample using a Hummer VI sputtering system from Anatech LTD., a commercial instrument used to plate surfaces with a conducting layer. Under deposition conditions used, the Au sputtering rate is approximately 125Å/minute. Deposition time is 20 minutes in order to achieve the nominal 2500Å overlayer. Post-sputtering depth profilometry measures the thickness of the Au layer to be 2900Å. This thickness is suitable for application as a sacrificial layer. As for the GaAs substrate material, previous Auger depth profile data yield a GaAs sputter etch rate of approximately 72Å/minute under present experimental conditions. After the GaAs/AlGaAs superlattice is sputtered during the analysis, ion beam bombardment continues for an additional 35 minutes in

order to achieve the extra 2500Å in crater depth. In this way, device layers to be measured are nominally forced to reside on the central portion of the crater sidewall, the region of constant bevel angle. The resulting depth profile of the analysis is identical to figure 4.19 with the exception of detection of the Au layer at the sample surface.

After completion of Auger depth profiling, Auger line scanning is performed across the beveled sidewall to measure the beveled thickness of relevant layers. Figure 4.21 is the resulting Auger line scan of In. The single InGaAs layer is clearly observed, and the full width-half maximum beveled thickness may be directly measured from the line scan output. Figure 4.22 is the Auger line scan plot of Al along the p-HEMT sidewall. The two AlGaAs layers documented in the device design are detected, as well as the broad superlattice layer. The decrease in Al signal intensity at a scan distance of approximately 10 μm corresponds to the absence of Al within the InGaAs film. The beveled film thickness of the GaAs/AlGaAs superlattice may be extracted from the data.

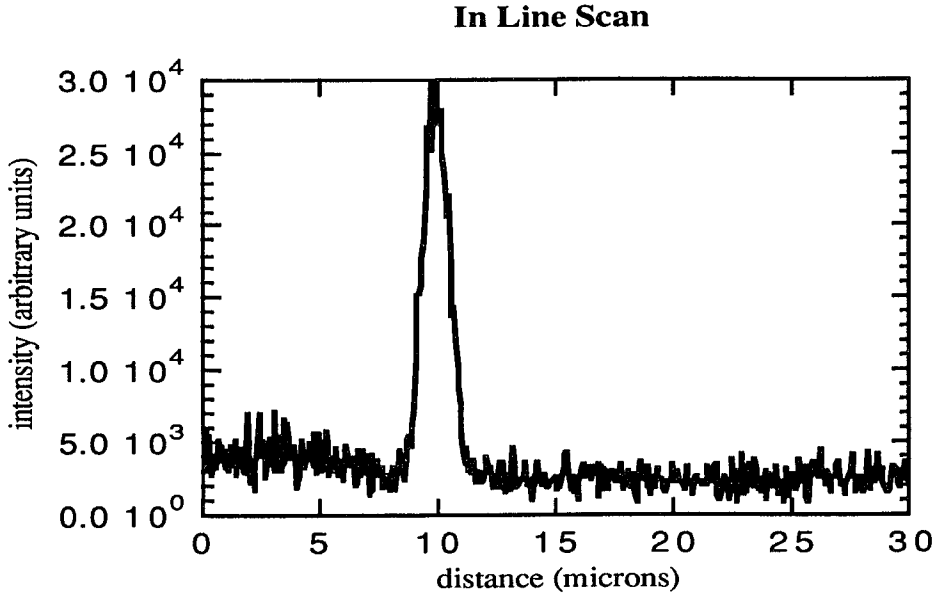

Figure 4.21 Auger line scan of In across p-HEMT sidewall

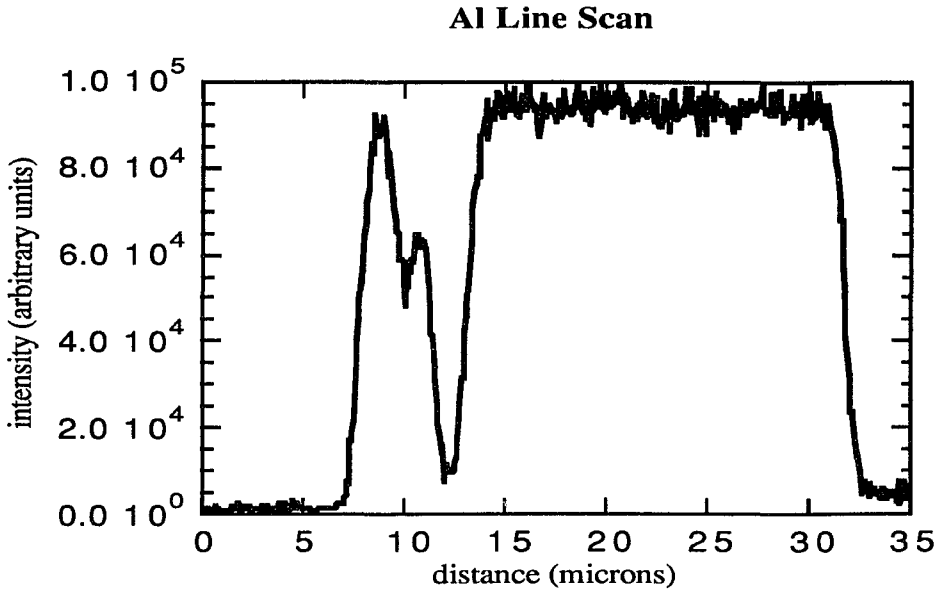

Figure 4.22 Auger line scan of Al across p-HEMT sidewall

Figure 4.23 is the Auger line scan plot of Ga across the crater sidewall. The

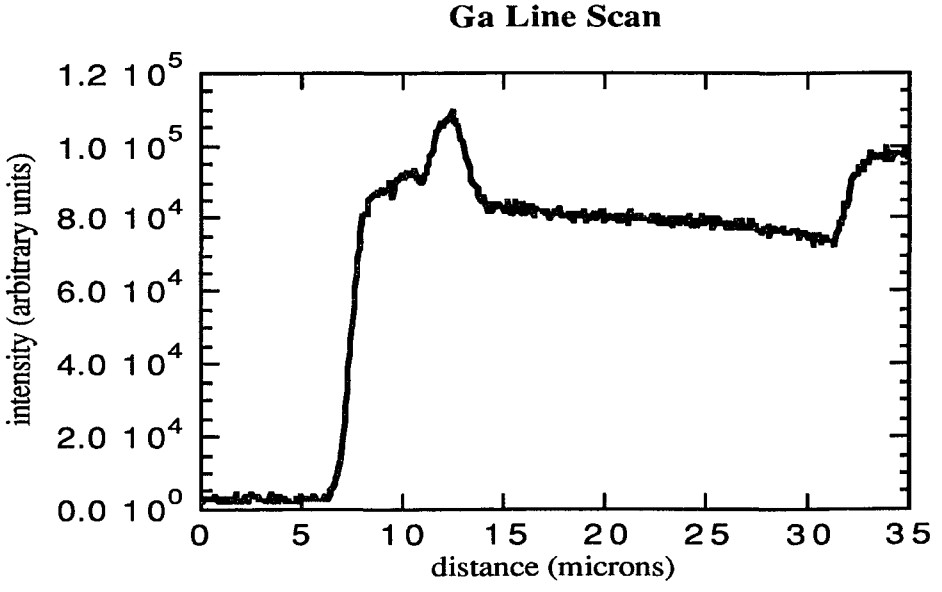

Figure 4.23 Auger line scan of Ga across p-HEMT sidewall

distinguishing feature of the plot is the intensity maximum at a scan distance of approximately 13 μm. This is associated with the extra GaAs layer detected in the Auger depth profile analysis. The beveled thickness of this GaAs film may be measured from line scan results.

Figure 4.24 is an SEM micrograph of the crater sidewall. Results of In and Ga Auger line scan experiments are vertically superimposed to aid in layer identification. Results of the Al line scanning are not included because incorporation of the Al plot results in difficulty in separating the three distinct elemental signals. The bright region at the top of the photograph is the deposited Au overlayer. The InGaAs layer is observed as a faintly distinct band of light contrast at a position corresponding to the maximum of the In line scan signal. The extra GaAs film detected in Auger depth profiling is more easily visible as a light contrast layer corresponding to the maximum of the Ga line scan signal. Characterized by darker contrast, AlGaAs sections are observed between the Au surface layer and the InGaAs film, between InGaAs and GaAs layers, and

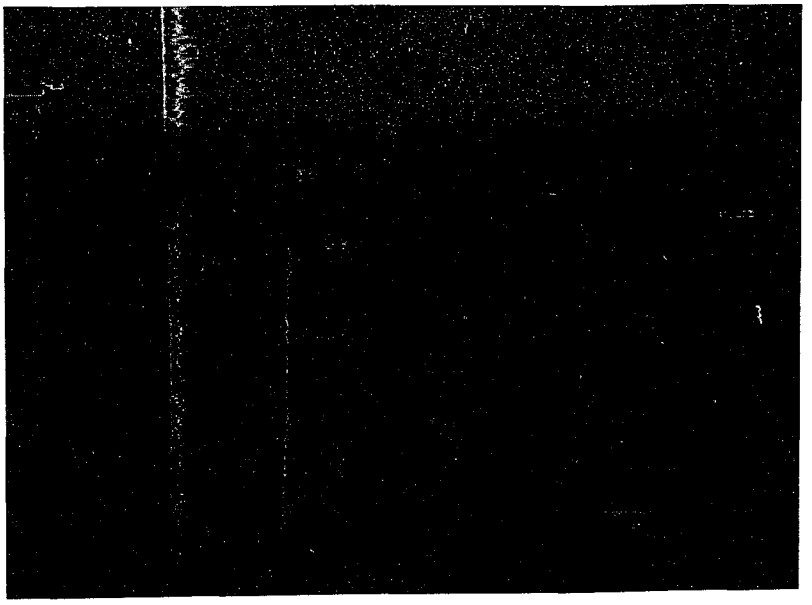

Figure 4.24 SEM image of beveled crater sidewall of p-HEMT

within the broad superlattice region. The rise in the Ga signal at the bottom of the photograph corresponds to the GaAs substrate. The substrate is not visible in the micrograph because inclusion of the micron marker omitted this region.

With the completion of line scanning measurements, depth profilometry measurements are performed to measure the bevel angle of the crater sidewall. Results of these measurements are illustrated in figure 4.25. Recall that the upper 2900Å on the crater sidewall are due to the deposited Au overlayer. Examination of figure 4.25 shows that sacrificial layer deposition is quite successful in confining device layers to the central region of the crater sidewall. At a crater depth of about 3000Å, the behavior of the sidewall is considerably more linear than the shallow region. Variation in the bevel angle is still evident at this depth, but the variation has certainly been decreased substantially. Furthermore, this linearity extends to a crater depth greater than 1 μm. Assuming that actual film thicknesses do not deviate greatly from nominal values, this indicates that all device films of interest reside in the central portion

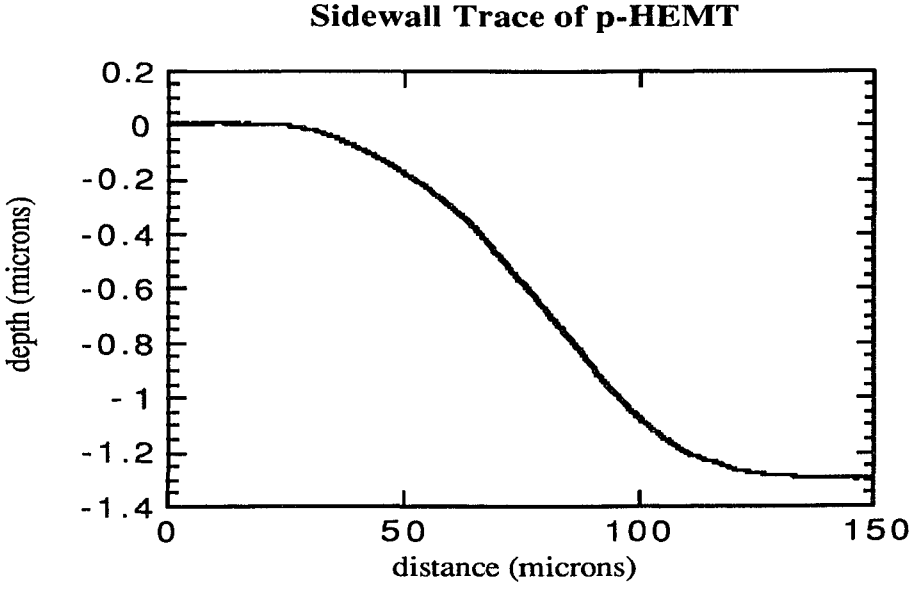

Figure 4.25 Depth profilometry trace of MMIC p-HEMT

of the sidewall, the region of constant bevel angle. In this initial attempt, overlayer deposition appears to be an effective technique for confining layers of interest within the sidewall region of constant bevel angle.

The constant bevel angle is calculated by the same procedure as in the previous section by identifying the linear region of the depth profilometry plot.

$\tan \alpha = M = (1.0268\ \mu m - 0.3524\ \mu m) / (97.26\ \mu m - 63.47\ \mu m) \rightarrow \alpha = 1.14°$

With beveled layer thickness measured by Auger line scanning and bevel angle measured from depth profilometry, actual film thicknesses are easily calculated. Table 4.5 summarizes the experimental results and lists layer thicknesses measured by TEM analysis. As in the TEM measurements on GaAs/InGaAs MQW in the previous section, the accuracy of TEM measurements is ±2Å. Referring to the design schematic in figure 4.18, the first AlGaAs layer in table 4.5 is a combination of the 350Å AlGaAs layer immediately following the n^+ GaAs cap, the first d-doped Si plane, and the subsequent 25Å AlGaAs film. TEM measurements indicate that this film compilation along with the n^+ GaAs cap layer is 500Å in thickness [34]. In the high-resolution TEM micrograph, the GaAs cap and the AlGaAs layer combination appear as a region of light contrast.

Table 4.5 Beveling Parameter Values for MMIC p-HEMT

Layer	Bevel Length L (μm)	Bevel Angle α (degrees)	Thickness d=L sinα (Å)	TEM Results (Å)
AlGaAs	2.65	1.14	530 ± 63	375 *
InGaAs	1.45	1.14	289 ± 47	132 ± 2
AlGaAs	1.05	1.14	209 ± 42	224 ± 2
GaAs	2.255	1.14	449 ± 58	500 ± 2
superlattice	21.48	1.14	4286 ± 308	4300 *

* Nominal design values

Distinction of GaAs and AlGaAs layers is not clear. Hence, direct TEM measurement solely of the sequence of AlGaAs layers is unavailable. This being the case, AlGaAs layer thickness derived by shallow angle beveling is compared to nominal layer thickness. The nominal thickness value is also used for the GaAs/AlGaAs superlattice because the superlattice sample foil resulting from thinning and ion milling in TEM sample preparation is not thin enough to measure thickness via TEM [33]. Thus, TEM thickness measurements of the superlattice are also unavailable. It is interesting that the first two films show large deviations from TEM results or nominal thickness values, but the final three layers are in agreement with TEM results or nominal values. This is probably due to error in the bevel angle value. It has previously been noted that despite the use of the Au overlayer, a small variation in the angle exists in the sidewall region adjacent to the Au surface layer. The constant bevel angle $\alpha=1.14°$ calculated from the central portion of the sidewall is, strictly speaking, not applicable to this region. Figure 4.26 illustrates the bevel angle variation with crater depth along the p-HEMT sidewall. This plot is generated by the same method described in the previous section, but 250Å increments are deployed rather than the 100Å steps used for the analogous GaAs/InGaAs MQW plot. Within the crater depth range of 0.3-0.4 μm, there is a wide variation in the bevel angle with depth. Because of this variation, the calculated constant bevel angle is not valid in this region. Consequently, calculated thickness measurements are in error. The final three layers in table 4.5 firmly lie within the region of constant bevel angle. Hence, associated thickness calculations for these films are in agreement with TEM measurements. In conclusion, the use of the sacrificial surface layer in this analysis does not result in confinement of the first two layers within the sidewall region of constant bevel angle. Nevertheless, in this first attempt, substantial decrease in angle variability has been gained through the

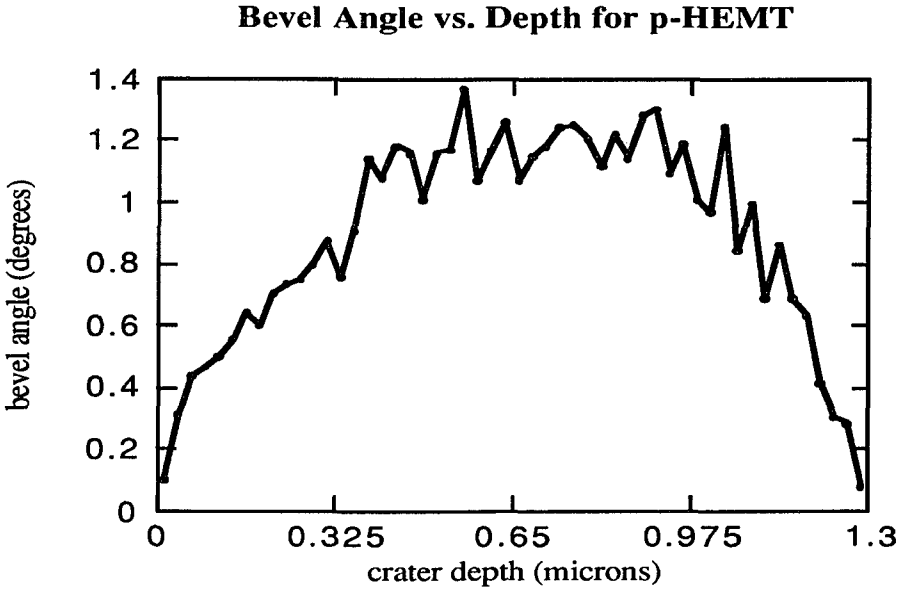

Figure 4.26 Variation of bevel angle with crater depth in p-HEMT

use of the Au overlayer. The use of this overlayer needs to be refined such that device layers are confined to the central portion of the sidewall with certainty. In future endeavors, overlayer studies will be performed in order to perfect the technique.

The size of the electron beam during the analysis should be verified to ensure the validity of the assumption that the beam dimension is smaller than that of the beveled layers probed. Electron beam size is measured by the same method outlined in the previous section. The result of the measurement is depicted in figure 4.27. The beam diameter is the difference between the points on the plot at 20% and 80% of maximum intensity. From this plot, the beam diameter is measured to be 5770Å. The beam size is thus verified to be nearly half the size of the smallest beveled film measured. From the previous assumptions, the electron beam model is thus valid.

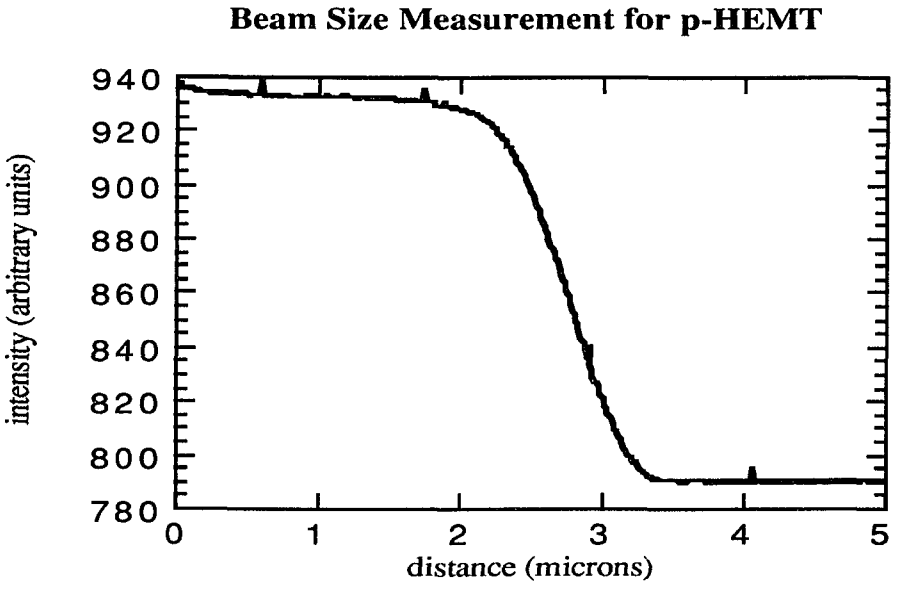

Figure 4.27 Electron beam diameter measurement

4.2 Metals

4.2.1 Pt/Si/Ti Ohmic Contacts

The Pt/Si/Ti materials system has been studied for application as an Ohmic contact to GaAs-based devices [37]. Briefly, the premise of current research is to deposit the system on p^+ GaAs and subject the composite structure to rapid thermal annealing (RTA). The goal is a reaction between Pt and Si to form a silicide, while the Ti, deposited as a diffusion barrier layer, maintains integrity to prevent reaction between the silicide and the GaAs substrate. This type of system has been demonstrated to exhibit Ohmic behavior at low contact resistances. A variety of annealing conditions have been investigated and subsequent electrical, chemical, and structural properties studied as a function of RTA conditions. Currently, research continues in this area of electronic devices.

The Pt/Si/Ti contacts have been studied extensively by Auger electron spectroscopy. The technique of shallow angle beveling for measuring film

thickness has been applied to these structures. The nominal structure is as follows: Pt(459Å)/Si(1260Å)/Ti(256Å)//GaAs. These are the resulting layer thicknesses obtained through depth profilometry measurement of each respective film. Figure 4.28 illustrates the results of Auger depth profiling on an as deposited Pt/Si/Ti//GaAs multi-layer structure. The signals are clearly labeled, and all layers are detected. Figure 4.29 is an Auger depth profile acquired under identical experimental conditions after the contact has been subjected to a 750°C, 10 second RTA. A number of differences are noted. Ga has out diffused from the substrate to the sample surface as a result of the RTA. Pt and Si have reacted in the annealed sample to form a silicide. There also appears to be an unreacted Si layer directly beneath the surface silicide. Ti and Si appear to be interdiffusing as well, possibly forming a silicide of Ti. At t=5 minutes, a second Pt signal hump is detected. Pt has diffused through the Si layer and has reacted with Si and Ti to form a complex alloy. In addition, As is diffusing into the Ti barrier layer. In fact, at approximately t=5.5 minutes, Pt, Si, Ti, and As are

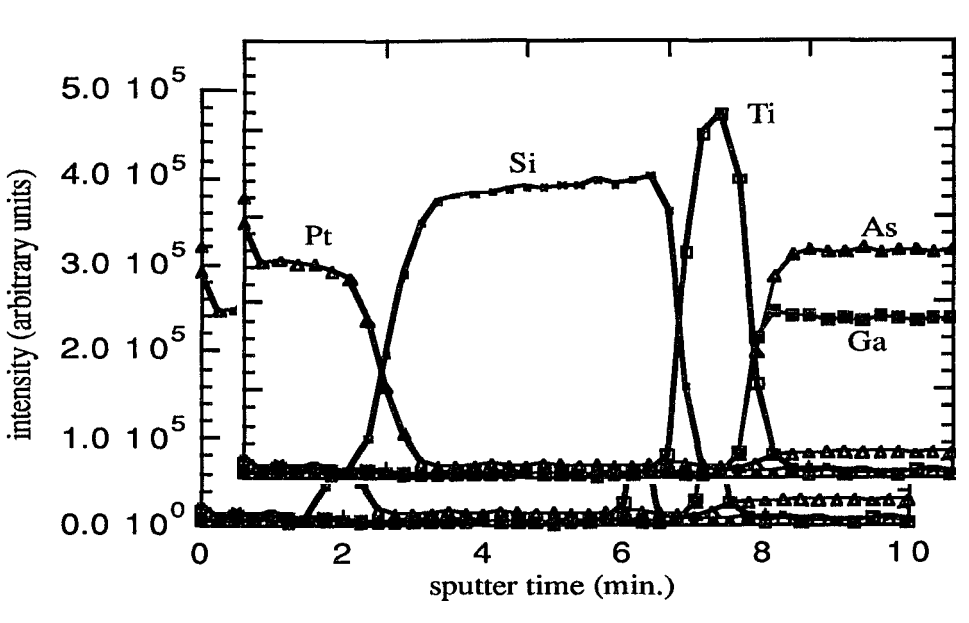

Figure 4.28 Auger intensity profile of as deposited Ohmic contact

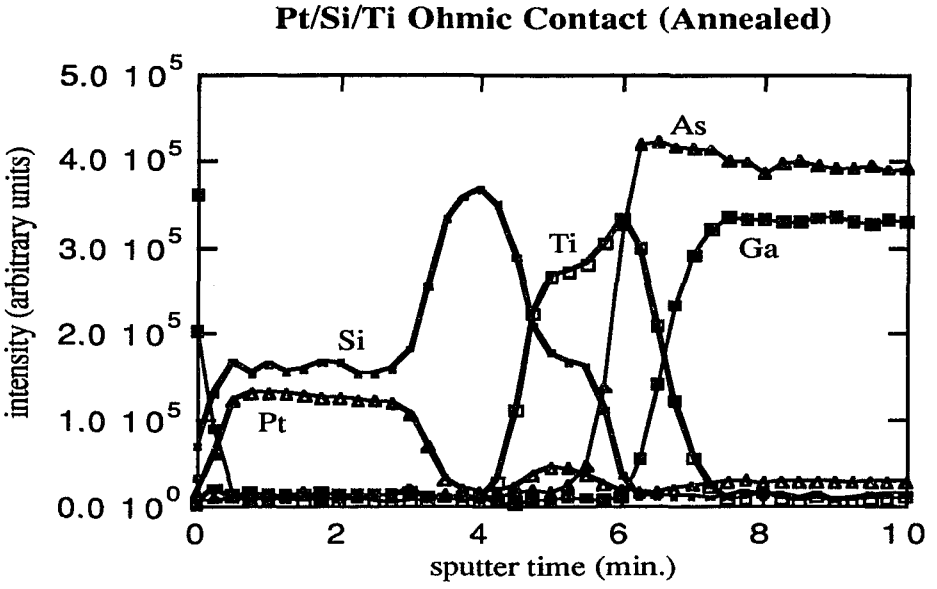

Figure 4.29 Auger intensity profile of annealed Ohmic contact

simultaneously detected at the same depth. In short, a great deal of interdiffusion and alloying takes place at these annealing conditions.

The resulting craters from the depth profile analyses are characterized by Auger surface mapping. The result is a striking pictorial display of interlayer diffusion brought on by RTA. Figure 4.30 shows four representations of the same field of view. Figure 4.30a) is an SEM image of the beveled crater produced by Auger depth profiling. The size of the crater bottom is 200 μm, as measured in the horizontal direction. Distinct layers are difficult to resolve in the micrograph. Figure 4.30b) is an Auger surface map of Pt within the region. The Pt film features a very shallow bevel angle, as the nominal 459Å layer appears quite broad in the Pt map. Figures 4.30c) and 4.30d) are Auger surface maps of Si and Ti respectively. Each layer is detected with a certain beveled thickness. For comparison, figure 4.31 consists of the corresponding fields of the annealed sample. The SEM image in figure 4.31a) shows a thin band of light contrast

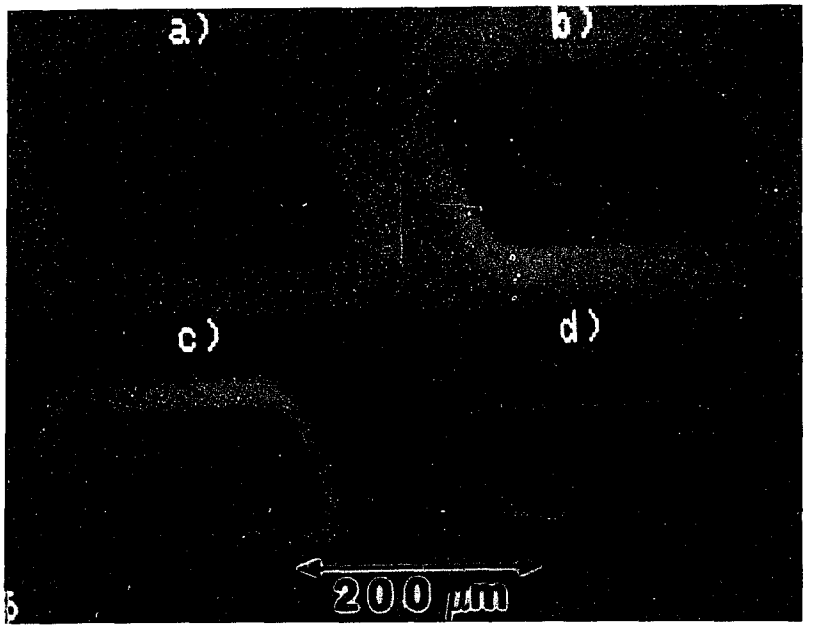

Figure 4.30 SEM image and surface maps of as deposited contact

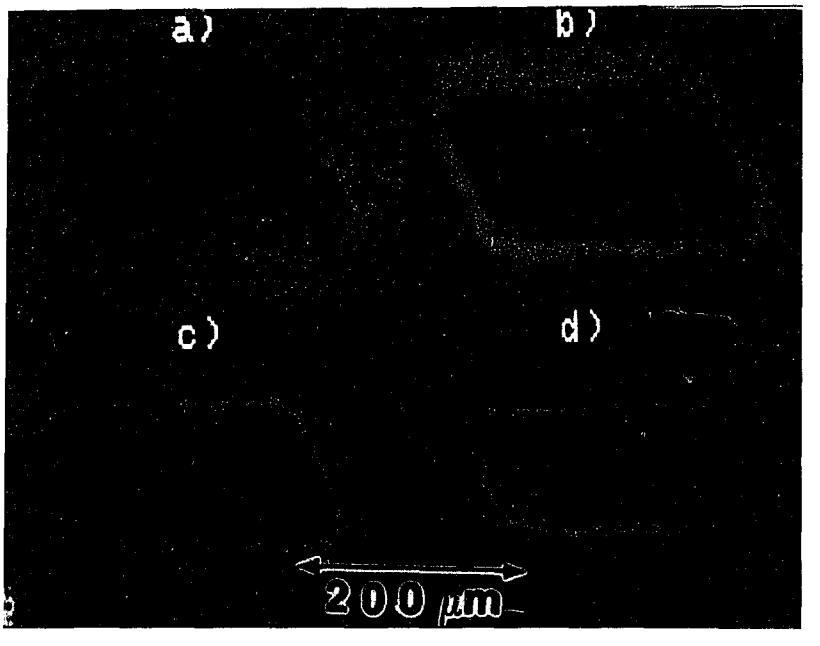

Figure 4.31 SEM image and surface maps of annealed contact

within the dark contrast band which is not present in figure 4.30a). The Auger surface map in figure 4.31b) identifies this thin band as Pt. The Si surface map in figure 4.31c) reveals the Si layer to have broadened from the as deposited case. In addition, distinct regions of silicide and unreacted Si are resolved. Figure 4.31d) shows the Ti barrier layer to have broadened as well. These observations are consistent with those inferred from the depth profile data. These analyses of the Ohmic contact demonstrate the utility of Auger surface mapping of beveled craters. The technique is a powerful tool for qualitatively studying interlayer diffusion and displays results in a striking manner.

After completion of surface map analysis, Auger line scanning is performed on the as deposited crater sidewall. The procedure of depositing a surface overlayer is not employed in this analysis. This being the case, the Pt layer at the sample surface will feature a variable bevel angle. Since thickness calculations under these conditions are invalid, the thickness of the Pt layer is not measured, and Pt line scanning is not performed. Figure 4.32 is the Auger line scan of Si

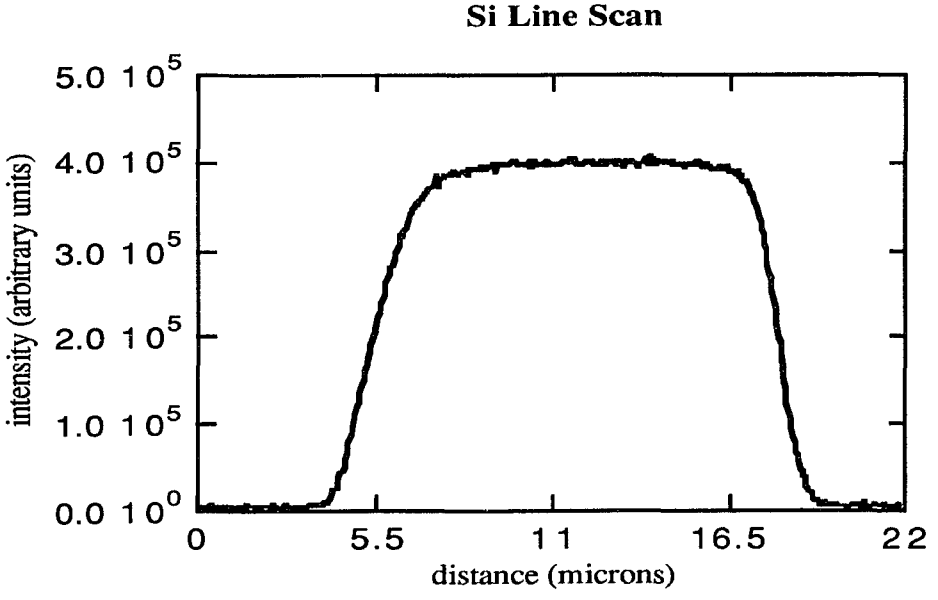

Figure 4.32 Auger line scan of Si across as deposited contact sidewall

along the crater sidewall. The broad beveled Si layer is readily detected. Figure 4.33 is the Auger line scan of Ti along the contact crater sidewall. Through analysis of the line scan data, beveled layer thicknesses are easily measured. Once the bevel angle is measured, film thicknesses may be calculated. Results of depth profilometry measurements are illustrated in figure 4.34. The trace detects several hillocks on the sample surface and crater bottom. More importantly, a nonlinearity occurs within the central portion of the crater sidewall at a crater depth of approximately 3000Å. The nature of this imperfection is unknown, and for the purposes of measuring the constant bevel angle, this portion of the sidewall is avoided. With the proper choice of sidewall area, the bevel angle calculation is as follows.

$\tan \alpha = M = (0.2099\ \mu m - 0.0501\ \mu m) / (61.11\ \mu m - 45.86\ \mu m) \rightarrow \alpha = 0.60°$

With the knowledge of the beveled layer thicknesses and bevel angle, film

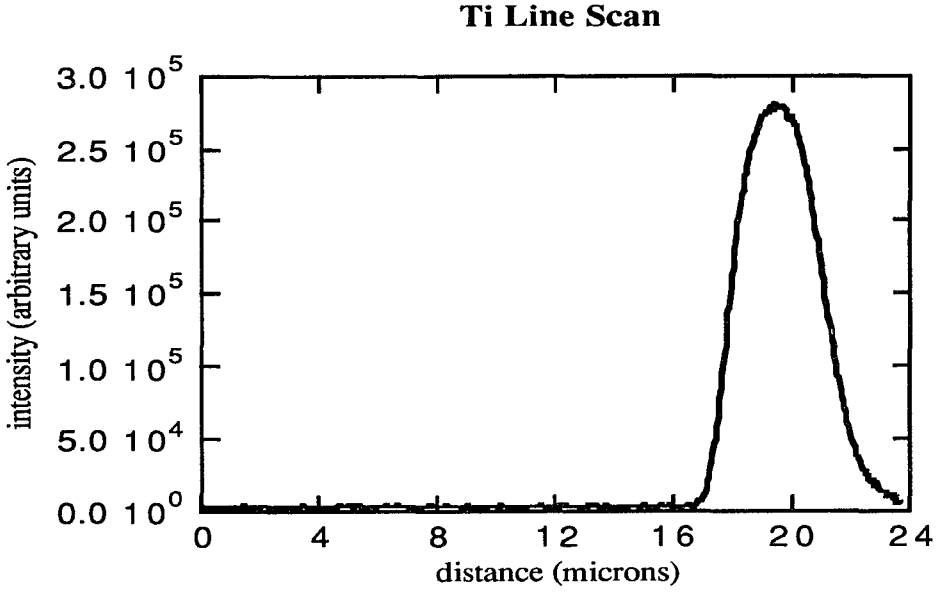

Figure 4.33 Auger line scan of Ti across as deposited contact sidewall

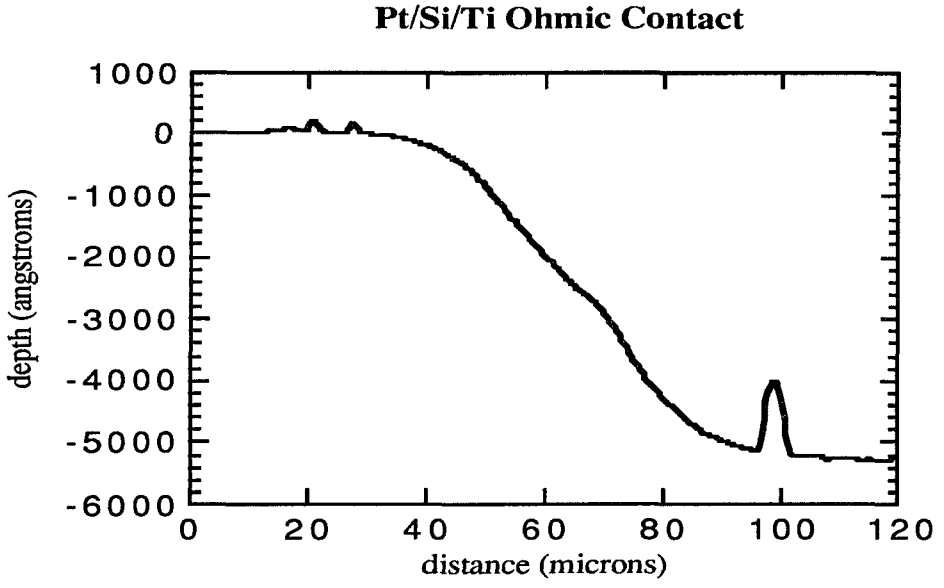

Figure 4.34 Depth profilometry trace of as deposited Ohmic contact

thicknesses may be calculated. Table 4.6 summarizes the results of the thickness calculations. TEM analysis is not performed on the Ohmic contact. Thus, thickness measurements derived by TEM analysis are unavailable. Uncertainties in the depth profilometry measurements are not available.

Contrary to previous results, there is a wider discrepancy between calculated layer thicknesses and nominal, or measured values. In this case, layer thicknesses determined by the beveling technique are compared to thickness values measured by stylus depth profilometry and not TEM measurements. Since depth

Table 4.6 Beveling Parameter Values for Pt/Si/Ti Ohmic Contact

Layer	Bevel Length L (μm)	Bevel Angle α (degrees)	Thickness d=L sinα (Å)	Profilometry Results (Å)
Si	14.51	0.60	1521 ± 204	1260
Ti	3.75	0.60	393 ± 64	256

profilometry is not nearly as accurate as TEM, some error may exist in the profilometry results as well. Also, it is known that metals exhibit a tendency to roughen when sputter etched with an ion beam [18]. If the beveled layer is topographically rough, the accuracy of Auger line scanning analysis is diminished due to the fact that a rough surface typically reduces the signal-to-noise ratio of the Auger signal. This leads to inherent inaccuracy in measured Auger electron intensity. Also, surface roughness reduces the accuracy of stylus depth profilometry that is used to measure the constant bevel angle along the crater sidewall. Since depth profilometry is a mechanical method in which a stylus is traced over the sample surface, it is intuitive that hillocks on the surface due to roughness degrade the accuracy of the stylus trace. These reasons may explain the inaccuracy of the calculated thickness of the Ti layer. However, this argument does not apply to the semiconducting Si layer. Additional studies shall be undertaken to address these questions. The first course of action is the analysis of the Pt/Si/Ti structure by TEM, since this is the authoritative method of accurately determining layer thicknesses. Thickness measurements can therefore be assessed by comparison to the highly accurate values derived by TEM analysis. Additional beveling studies are fruitful as well in order to determine if the measured thicknesses are reproducible. If lack of experimental precision is found, the cause must be ascertained.

Electron beam size measurements are not performed for the Pt/Si/Ti Ohmic contact. Previous results show that the electron beam diameter is less than 6000Å during Auger line scan analysis. Since each line scan is performed under identical conditions, the beam diameter should not fluctuate to a great degree. Since the Si and Ti beveled films are considerably thicker than ~ 6000Å, it is assumed that the beam diameter is less than the beveled thickness of probed films and all associated assumptions in the beam scanning model are valid.

In conclusion, despite deviation between thicknesses derived by this research work and depth profilometry, shallow angle beveling is found to apply to metals as well as semiconductors. In addition, when used in conjunction with Auger surface mapping, results illustrate that the beveling technique is valuable for qualitative interlayer diffusion and uniformity studies, as well as convincing two dimensional graphical displays.

4.3 Insulators

4.3.1 SiO_2/Si_3N_4 Superlattice Layers

The shallow angle beveling technique is applied to a SiO_2/Si_3N_4 superlattice structure. The superlattice is used to study the degree of reaction between adjacent SiO_2 and Si_3N_4 films. Information obtained from this study is useful for fabrication of silicon oxynitride (SiON) films in which the resulting graded refractive index of the film is modeled as a combination of the respective indices of refraction of SiO_2 and Si_3N_4 [11]. Since measured refractive index is a strong function of elemental composition, chemical analysis of these multi-layer structures is required. Ultimately, SiON films in which the index of refraction is precisely graded are used in optical waveguide applications.

The superlattice structure is fabricated by plasma-enhanced chemical vapor deposition (PECVD). The nominal structure consists of 7 periods of SiO_2(200Å)/Si_3N_4(200Å). An additional 200Å of SiO_2 is deposited between these 7 periods and the Si substrate. In all, 15 layers of alternating SiO_2/Si_3N_4 films are deposited. At a nominal thickness of 200Å, the total thickness of the structure is 3000Å. Thickness measurements are not performed on the sample, but through calibration of the PECVD system and prior thickness studies, the total thickness of 3000Å is accurate to ±90Å [38].

The superlattice structure is analyzed by Auger depth profiling. For this

analysis, no Au overlayer is deposited upon the structure. Results of the analysis are illustrated in figure 4.35. All signals are clearly labeled. Distinct layers are resolved by oscillations in the O and N signals. The Si signal appears to replicate the N signal, but at a decreased intensity. This is consistent with the fact that there is a higher atomic concentration of Si in nitride layers than in the oxide layers. Therefore, the Si signal should achieve a local maximum intensity within a nitride layer situated between two oxide layers, which is readily observed in figure 4.35.

A beveled sputter crater is produced as a result of Auger depth profiling. Figure 4.36 is an SEM image of the crater. Alternating beveled layers are clearly observed. Bands of light contrast are SiO_2 layers and dark contrast bands are Si_3N_4 films. The striking contrast between alternating films may be due to a pronounced difference in composition between SiO_2 and Si_3N_4. The dark nitride band at the top of the sidewall appears thicker than subsequent layers. Likewise, the light contrast oxide band nearest to the crater bottom appears

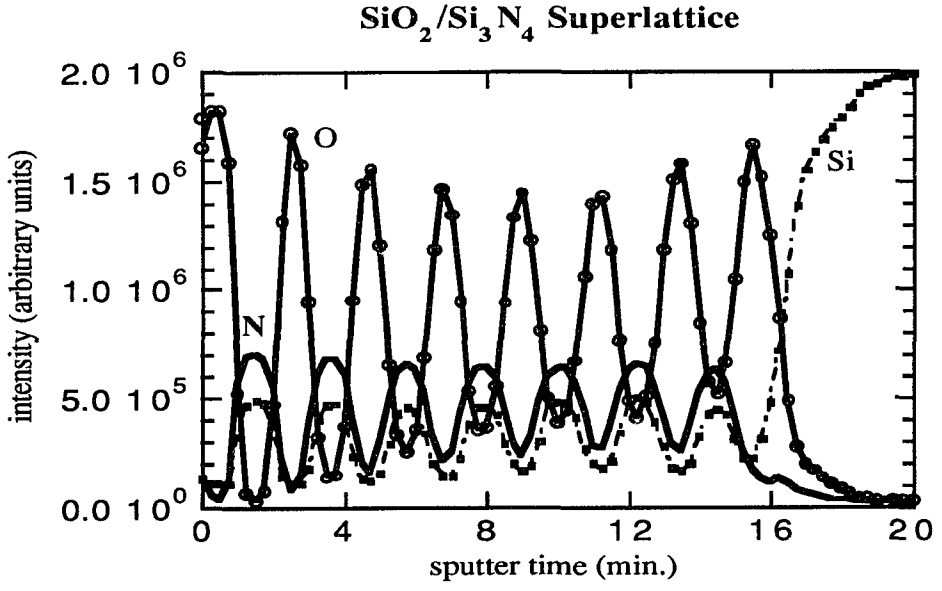

Figure 4.35 Auger depth profile of SiO_2/Si_3N_4 superlattice

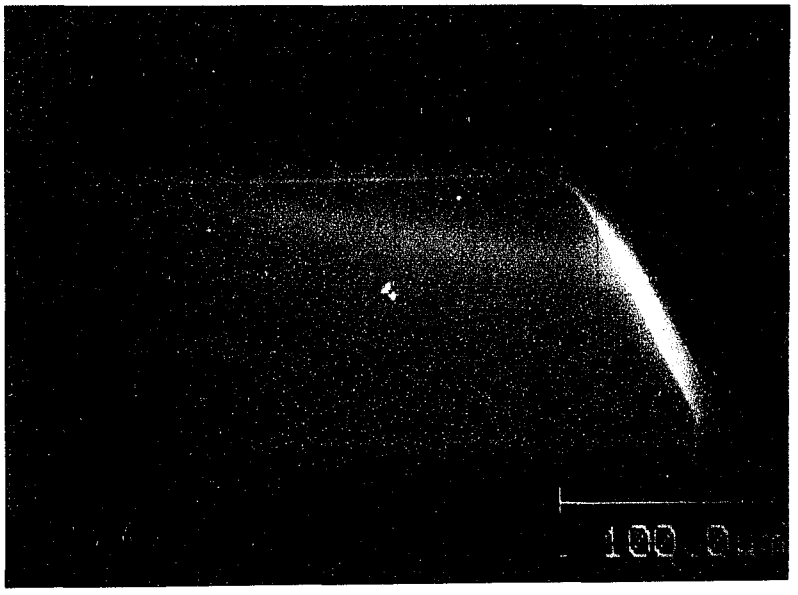

Figure 4.36 SEM image of beveled SiO_2/Si_3N_4 superlattice

thicker than preceding oxide layers. This is a manifestation of the bevel angle decreasing significantly at the top and bottom portions of the crater sidewall, as has been observed in previous sections. At any rate, insulating films of 200Å nominal thickness are easily resolved at relatively low magnification, implying a shallow sidewall bevel angle which decreases further at the sidewall top and bottom.

Auger line scanning is subsequently performed along the beveled sidewall. O and N signals are monitored in the analysis. Figure 4.37 is the result of the Auger line scan of O. Signal oscillations corresponding to distinct layers are readily observed. Observation of the Auger depth profile of figure 4.35 indicates 8 distinct SiO_2 layers. Eight O maxima are observed in the line scan data if the surface oxide is included. That is, an O maximum exists at a scan distance of zero, corresponding to the first SiO_2 film at the sample surface. Figure 4.38 is the result of the Auger line scan of N along the superlattice

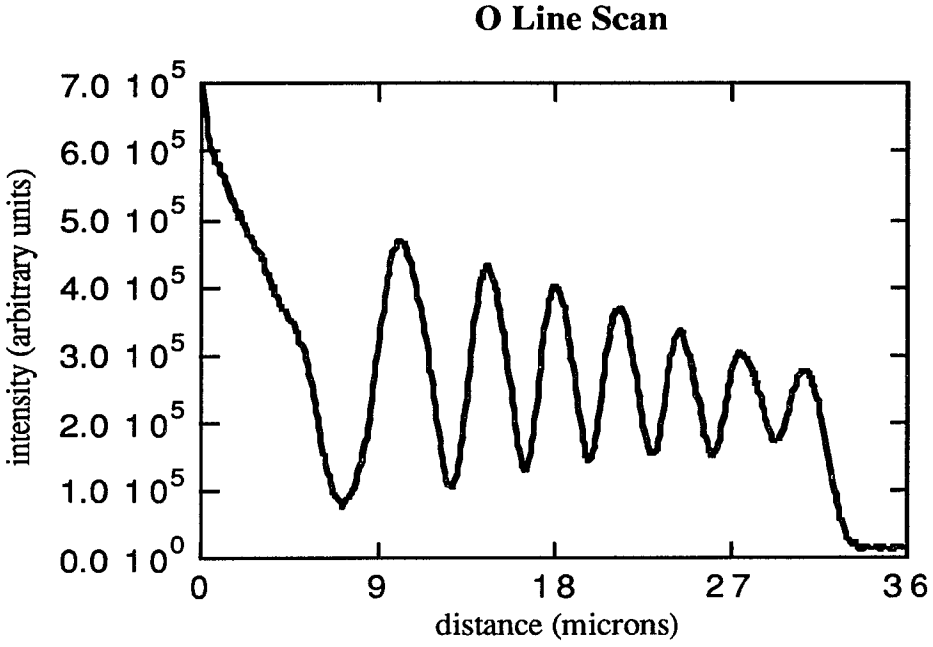

Figure 4.37 Auger line scan of O along superlattice sidewall

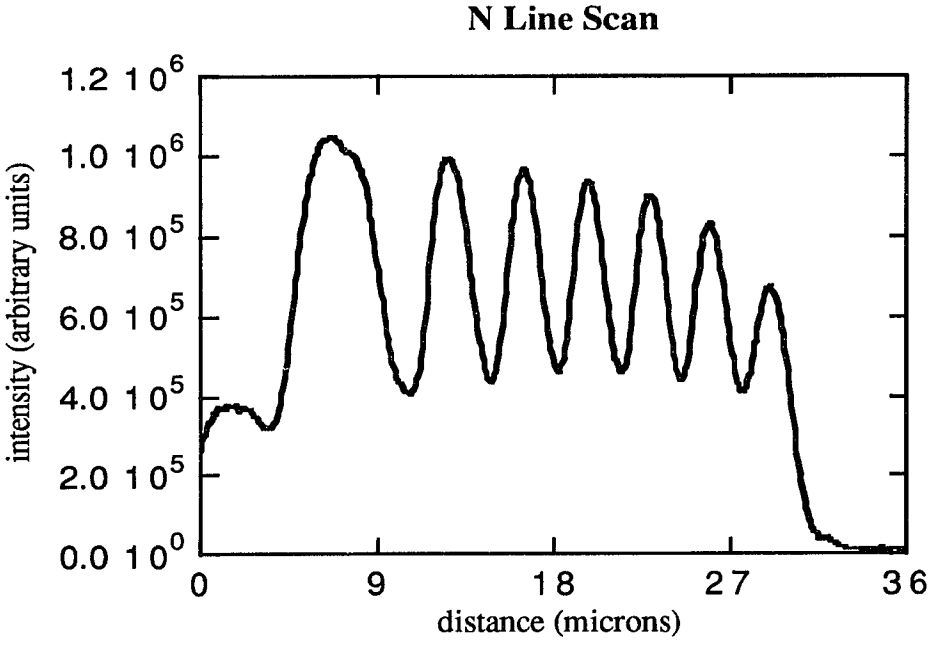

Figure 4.38 Auger line scan of N along superlattice sidewall

sidewall. This line scan reveals 7 N signal maxima, in agreement with the 7 Si_3N_4 layers detected in the depth profile. Results of the line scans appear qualitatively similar. However, superposition of the O and N line scan plots show that O signal maxima occur at N signal minima, corresponding to the center of an SiO_2 layer. The reverse case is true as well, namely, N signal maxima occur at the same point as O signal minima, corresponding to a nitride layer. This is clearly illustrated in figure 4.39, a magnified SEM image of the beveled crater sidewall with O and N line scans vertically superimposed upon the image. The 15 alternating layers are resolved. The micrograph shows that O signal maxima occur in bands of light contrast and N maxima occur in bands of dark contrast. Furthermore, maxima of one signal coincide with minima of the other signal. In short, alternating SiO_2 and Si_3N_4 are unambiguously resolved. Through Auger line scanning, beveled layer thicknesses are measured.

Depth profilometry analysis is performed to determine the constant bevel angle. Results of depth profilometry measurements are given in figure 4.40. The

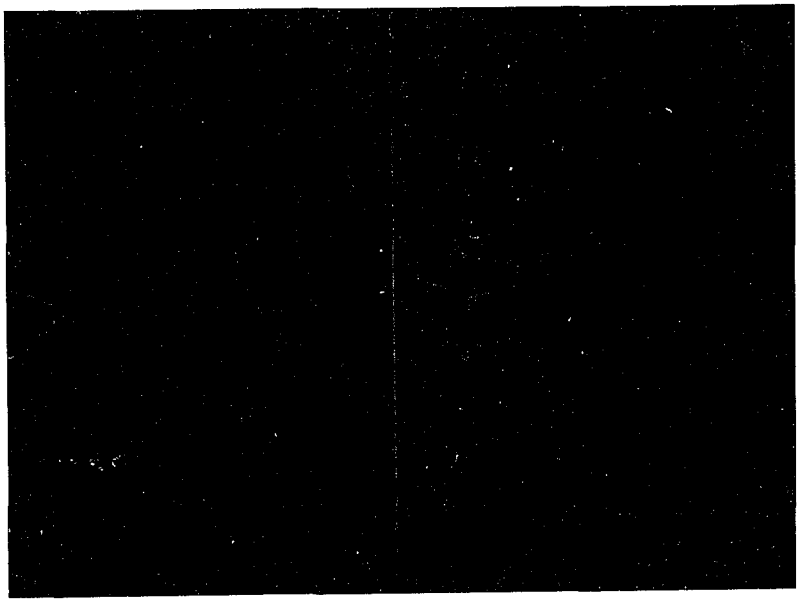

Figure 4.39 SEM image of beveled sidewall with line scan signals

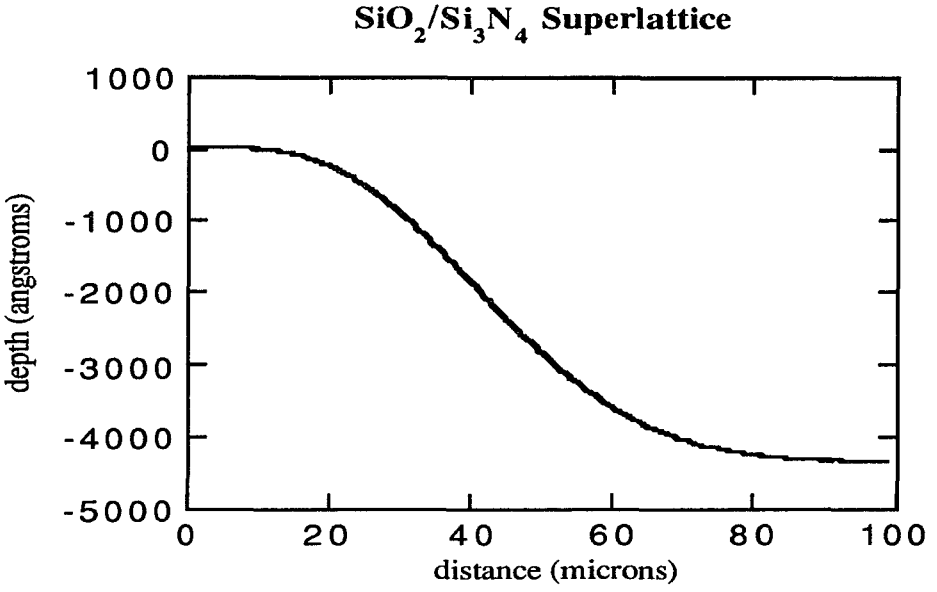

Figure 4.40 Depth profilometry trace of superlattice sidewall

trace is similar to those previously reported. A region of constant bevel angle exists in the central portion of the crater, and the angle decreases at the top and bottom of the sidewall. The constant bevel angle is determined as follows:

$\tan \alpha = M = (0.2514\ \mu m - 0.1212\ \mu m) / (57.11\ \mu m - 44.25\ \mu m) \rightarrow \alpha = 0.58°$

With beveled thicknesses and bevel angle known, film thicknesses may be determined. Table 4.7 summarizes the results of film thickness calculations. Due to the variability of the bevel angle along the top and bottom portions of the sputter crater, the first five layers and final two layers in the structure are excluded. That is, the first two SiO_2/Si_3N_4 periods and next SiO_2 layer are omitted from table 4.7. Furthermore, the final SiO_2 and Si_3N_4 layers are excluded from calculation as well. The constant bevel angle is applicable to the remaining 8 layers within the central portion of the sidewall, and as such

Table 4.7 Beveling Parameter Values for SiO_2/Si_3N_4 Superlattice

Layer	Bevel Length L (μm)	Bevel Angle α (degrees)	Thickness d=L sinα (Å)	Nominal Thickness(Å)
Si_3N_4	2.01	0.58	204 ± 40	200
SiO_2	2.10	0.58	212 ± 42	200
Si_3N_4	1.89	0.58	191 ± 39	200
SiO_2	1.93	0.58	195 ± 39	200
Si_3N_4	1.80	0.58	182 ± 38	200
SiO_2	1.93	0.58	195 ± 39	200
Si_3N_4	1.84	0.58	187 ± 38	200
SiO_2	2.05	0.58	208 ± 41	200

thickness calculations are performed for these films. Results of thickness calculations are in excellent agreement with nominal values. The technique of shallow angle beveling for measuring film thicknesses is thus applicable to insulating SiO_2/Si_3N_4 superlattices. The technique is proven to apply very well to thin insulating layers provided that multi-layer structures are not resistive to the point where sample charging invalidates thickness measurements. The most severe sample charging occurs during analysis of bulk insulators or thick (> 2 μm) insulating films. Beveled thickness of such samples cannot be measured through Auger line scanning. The effects of sample charging are reported in the experimental section of this presentation.

As in the previous section on Pt/Si/Ti Ohmic contacts, electron beam diameter measurements are not performed. Since all Auger line scan measurements are performed under identical experimental conditions, the assumption is that the beam diameter is less than 6000Å. This assumption is based on beam size measurements performed for the GaAs/InGaAs MQW and MMIC p-HEMT systems. Since the thinnest beveled layer probed in the superlattice is greater than 1.5 μm in thickness , the electron beam diameter is observed to be smaller than this critical thickness. With this assumption, beam diameter measurements need not be performed.

4.3.2 Infrared Optical Filter

Shallow angle beveling by an ion beam is applied to an infrared (IR) optical filter. The filter is fabricated as part of an independent project [39]. The resultant sputter crater produced by SIMS analysis is observed to be beveled. It is noted that the beveled crater is produced in a different system by another analysis technique than the previously analyzed multi-layer structures. Nevertheless, like Auger depth profiling, SIMS depth profiling chemically characterizes samples as a function of depth by sputter etching the sample with an ion beam. The effect of beveling device structures is the same under SIMS analysis. In this respect, once the crater is formed, subsequent Auger analysis may be performed on the beveled crater sidewalls.

The IR filter consists of alternating Si and Al_2O_3 films, with a thin Al layer symmetrically incorporated in the middle of the device structure. Figure 4.41 is a nominal device schematic of the filter design. Documented thicknesses are acquired in-situ through quartz crystal oscillator measurements during filter fabrication.

The beveled crater sidewalls are analyzed by Auger surface mapping. The goal of the analysis is verification of the presence of all multi-layers. Thus, line scan analysis for thickness measurement of beveled films is not performed. Results of Auger map analysis are depicted in figure 4.42. Figure 4.42a) is an SEM image of the resulting sputter crater after SIMS depth profiling. The area of the crater bottom is 400 μm x 400 μm. The crater sidewall features areas of distinct contrast. Figure 4.42b) is an Auger surface map of O within the SEM field of view. Thin dark bands along the sidewall indicate areas of low O concentration relative to surrounding regions. Figure 4.42c) is a chemical map of Al in the same region. This map appears to be similar to the O surface map, including the occurrence of dark bands located at approximately the same points

Al_2O_3	1561Å
Si	1315Å
Al_2O_3	3521Å
Si	1576Å
Al_2O_3	6003Å
Al	285Å
Al_2O_3	5926Å
Si	1679Å
Al_2O_3	2968Å
Si	1565Å
Al_2O_3	2485Å
Si	1642Å
Si substrate	

Figure 4.41 Design schematic of IR filter

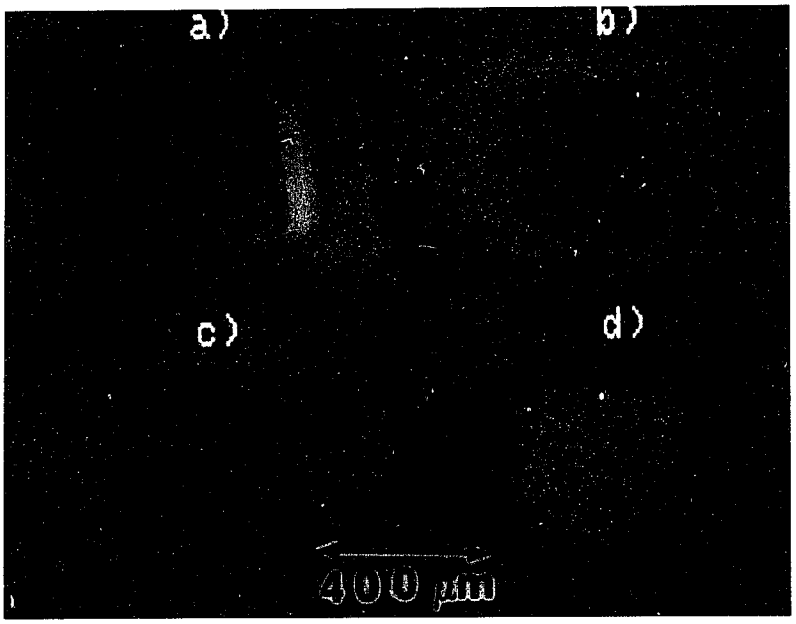

Figure 4.42 SEM image and surface maps of IR filter

as in the O map. Figure 4.42d) is an Auger surface map of Si. The thin bands which appear dark in the O and Al analyses are observed to be light in the Si analysis. In addition, the crater bottom is characterized by a high intensity Si signal. From these results, it is clear that the bands of light contrast in the SEM image are Si layers and darker contrast bands are Al_2O_3 films. Auger surface mapping has enabled chemical identification of the various layers observed in the SEM image. Furthermore, the presence of all layers in the nominal filter design are observed in the data. For example, in viewing the crater sidewall on the right side of figure 4.42c), the Al chemical map, the surface layer is seen to be Al_2O_3. In sequence, the following layers are Si, Al_2O_3, and Si respectively. The next film is detected as a continuous Al_2O_3 layer, but is actually comprised of the central Al layer and two adjacent Al_2O_3 layers. The following layers are observed to be Si, Al_2O_3, Si, and Al_2O_3. The final Si layer deposited onto the substrate is not observed in the chemical data, but the SEM image detects a final band of bright contrast adjacent to the crater bottom, the Si substrate. This is interpreted to be the final Si film in the device structure. Therefore, all device layers are present and accounted for.

Through the use of shallow angle beveling, distinct layers of the IR filter have been observed and chemically identified. The technique is thus viable for characterization of insulating layers, provided analysis artifacts due to sample charging do not ensue.

As a final note to the ion beam beveling phenomenon, it has been observed throughout this work that the constant bevel angle measured within the central portion of a particular crater sidewall varies with crater depth within numerous craters. This has been clearly demonstrated in the GaAs/AlGaAs MQW structures in section 4.1.1. In general, a deeper sputter crater results in a greater bevel angle. The variation of bevel angle with crater depth sampled from

a variety of analysis craters is plotted in figure 4.43. The data points in the plot represent a variety of constant bevel angles measured within different craters generated in semiconducting, metallic, insulating, and ferroelectric [40] samples. Thus, the plot describes the observed trend over a wide classification of materials. The plotted points lie reasonably close to a least-squares line superimposed on the graph. From this initial data, as a first-order approximation, it appears that bevel angle varies linearly with crater depth. The computer-generated, least-squares line has the equation:

$$\alpha = 1.065d - 0.0139$$

Thus, the data indicates that within a crater depth range of ~ 0.01 μm to approximately 2.5 μm, the constant bevel angle value measured in the central region of the crater sidewall is a linear function of the total crater depth. This is a useful relation which shall be verified in future work through more exhaustive

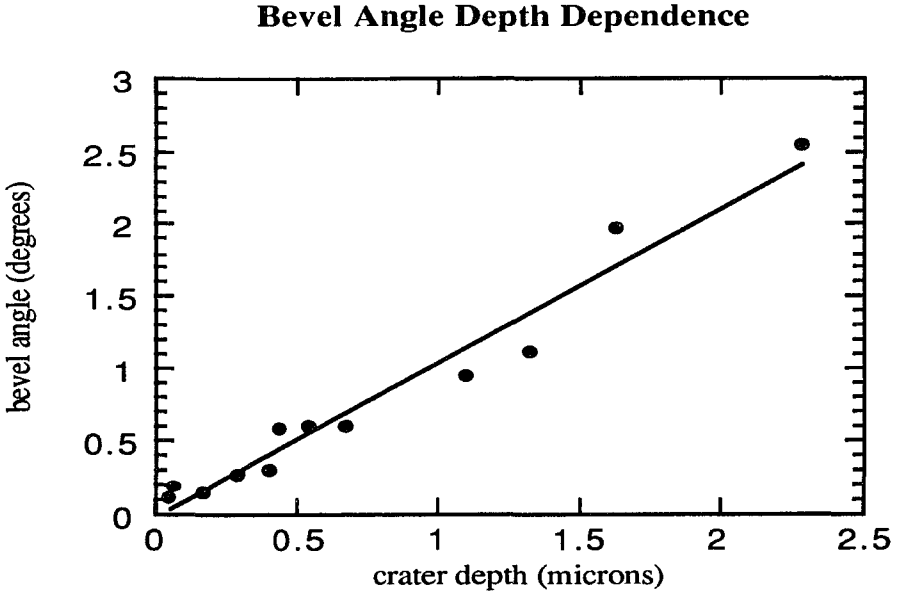

Figure 4.43 Dependence of constant bevel angle on crater depth

measurements. In addition, constant bevel angles shall be measured within deeper craters in order to extend the domain of crater depths to which this relation, or possibly a more refined relation, is applicable.

4.4 Chemical Etching

The shallow angle beveling technique proposed in this research is suitable for measuring film thicknesses as small as ~ 100Å. For some applications, the critical issue is not absolute thickness measurements, but resolution of ultrathin layers and relative thicknesses between these layers. The ability to conclusively resolve very thin films is qualitatively valuable in verifying the presence of layers in nominal device designs. In addition, relative thickness measurements between resolved layers are useful in correlating structural characteristics of devices with their performance. For example, multiple quantum well systems have been extensively studied in this research. Observation that one or more quantum wells differ in thickness from other wells may help explain deviations in electrical or optical properties from theoretical behavior. Furthermore, the ability to resolve thin films and provide relative thicknesses over a large area aids in probing the degree of lateral uniformity in film growth processing and subsequent device structures produced as a result thereof.

It has been discovered that subjecting ion beam bevel etched samples to a suitable chemical etch results in enhancement of crater sidewall features, facilitating resolution of thin films [30]. The strategy is to chemically etch one particular material within the structure in order to emphasize layer contrast, increasing the ability to resolve adjacent layers relatively immune to the etchant.

Systems studied by this method include the GaAs/InGaAs MQW and a p-HEMT device. Samples are etched in a 1:1 bleach (5% sodium hypochlorite) - deionized (DI) water solution for 5 seconds, rinsed in DI water and blown dry

with filtered nitrogen gas. The etchant is chosen because it is preferential to GaAs [30]. That is, the etchant removes GaAs and leaves AlGaAs and InGaAs layers intact. Strictly speaking, the etchant attacks each of these layers, but the etch rates of AlGaAs and InGaAs in this solution are considerably less than that of GaAs. Effectively, the AlGaAs and InGaAs layers remain while the GaAs is removed.

Optical microscopy using a green interference filter is performed on post-chemically etched beveled craters. To illustrate the effect of chemical etching on the crater sidewalls, an optical photograph of a p-HEMT device after chemical etching is provided in figure 4.44. The device structure is similar to that of the p-HEMT studied in section 4.1.3 of this research. There is a GaAs cap layer at the sample surface, followed in sequence by AlGaAs, InGaAs, and AlGaAs layers. The most notable feature is an AlGaAs(200Å)/GaAs(18Å) superlattice of periodicity 10. The dark region at the crater bottom is the GaAs substrate after etching. This material appears to be topographically rough, a manifestation of an

Figure 4.44 Optical photograph of post-etched p-HEMT sidewall

etching process. It is evident that such a chemical treatment enhances contrast between device layers within the AlGaAs/GaAs superlattice. Comparison of figure 4.44 with the SEM image of the unetched beveled crater of figure 4.20 shows the dramatic improvement in layer delineation within the AlGaAs/GaAs structure. In the SEM image prior to chemical etching, the crater sidewall is smooth and featureless within the superlattice layer. In chemically etching the crater, GaAs layers are removed between AlGaAs layers. Since AlGaAs layers remain relatively unaffected, sequential layers of GaAs between adjacent AlGaAs layers are removed. With the removal of GaAs films, the result is a staircase structure of AlGaAs layers along the portion of the sidewall corresponding to the superlattice region. This modification in surface topography creates distinct features on the crater sidewall and enhances contrast between layers. In this way, resolution of thin layers is accomplished. Despite the fact that the GaAs has been removed, a small step is created where the GaAs layer resides, and this step is indicative of a layer 18Å in thickness. Such ultrathin layers are resolved through the contrast enhancement offered by chemical etching.

GaAs/InGaAs MQW structures are also investigated in this initial study. This is the same system investigated in section 4.1.2 for layer thickness measurements. However, it is noted that this is not the same physical sample as in section 4.1.2. Respective InGaAs layers in this sample have a higher In mole fraction than those in which thickness measurements are performed. Nevertheless, the same nominal structure applies, namely four periods of GaAs(200Å)/InGaAs(100Å) on a GaAs substrate. The beveled craters are etched using the same etchant under identical conditions as previously described. As an illustration of the pronounced effect of chemical etching on the crater sidewall, an optical photograph of the beveled crater prior to chemical etching is provided in figure 4.45. As has been noted, the crater is featureless and distinct

GaAs and InGaAs layers are not resolved. Figure 4.46 is an optical micrograph of the same sample after chemical etching. The difference in layer resolution is striking. As in the case of the p-HEMT, the GaAs substrate appears visibly rough in comparison to the unetched crater. It seems that only three InGaAs layers are detected on the crater sidewall rather than the nominal four layers. This is due to removal of the surface GaAs layer as a result of chemical etching. The sample surface in figure 4.46 is actually the first InGaAs layer in the MQW structure. Auger spectral analysis shows this to be the case. The first step observed at the top of the crater sidewall corresponds to the location of the second GaAs layer prior to chemical etching. The remaining InGaAs layer and following two periods of GaAs/InGaAs are clearly observed. Creation of steps as a result of GaAs layer removal provides topographical features enabling resolution of thin layers. Furthermore, the first InGaAs layer below the sample surface appears to be greater in thickness than subsequent layers. As has been previously noted, this is due to the variable bevel angle along the crater sidewall.

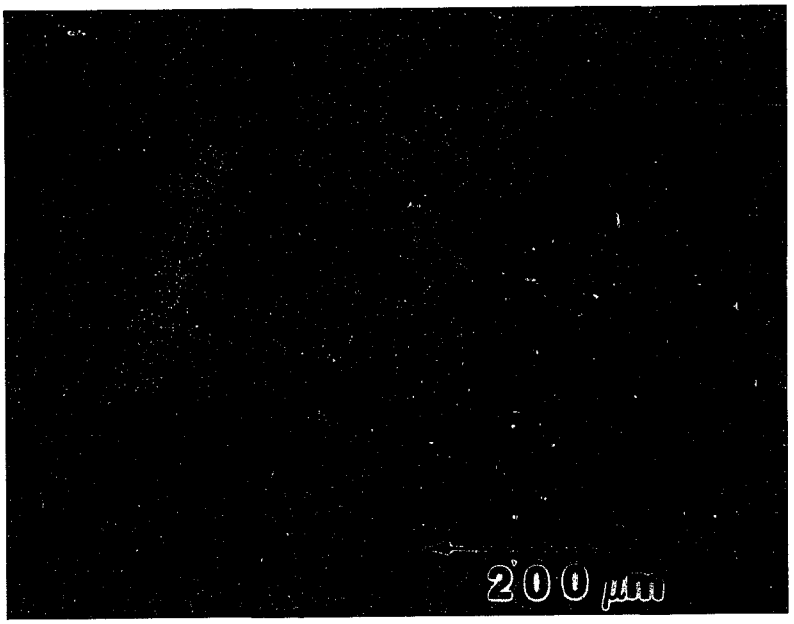

Figure 4.45 Optical photograph of GaAs/InGaAs MQW prior to etch

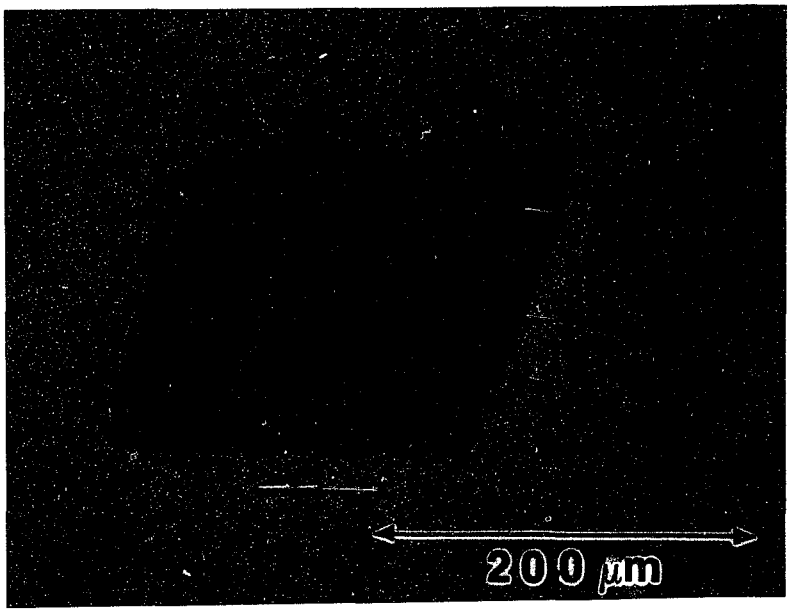

Figure 4.46 Optical photograph of GaAs/InGaAs MQW after etch

The final pair of InGaAs layers lie within the sidewall region of constant bevel angle. Thus, they appear to be approximately the same beveled thickness.

In conclusion, chemical etching of ion beam beveled craters enhances sidewall features through topographical modification. By producing steps on the crater sidewall corresponding to chemically etched layers, resolution of thin films is readily achieved. In the case of the p-HEMT structure, steps associated with 18Å GaAs layers are easily observed.

CHAPTER 5

CONCLUSION AND FUTURE WORK

Shallow angle beveling of multi-layer structures has been found to be a straightforward method of measuring thicknesses of thin films. The technique is conceptually simple and may be performed in a matter of hours. Film thicknesses on the order of ~ 100Å have been measured. In addition, adjacent films of sufficiently different contrast have been resolved by scanning electron microscopy. For distinct films of similar contrast, Auger chemical mapping has been used in conjunction with shallow angle beveling, providing a graphical display of device structures which is valuable for qualitative study of film uniformity and interlayer diffusion. Chemical etching of beveled structures greatly enhances crater sidewall features so that ultrathin films are resolved by optical microscopy. The presence of films on the order of 20 Å has been detected. The goal of the technique is to ultimately develop the capability of measuring film thicknesses less than 100 Å with much greater accuracy than what is presently achieved. Through systematic study of the issues of shallow angle beveling by an ion beam, this goal will hopefully be realized in the near future.

Many issues remain to be addressed in refining the technique of measuring thicknesses derived by the shallow angle beveling phenomenon. At present, validity of the procedure rests on the assumption that the electron beam used in scanning beveled layers to measure apparent thicknesses resembles a perfect Gaussian distribution. It is this assertion which enables measurement of beveled film thicknesses to be precisely the full width-half maximum of the elemental Auger signal in question, without accounting for the finite size of the electron beam [32]. Such an assumption shall be properly tested. The electron beam

intensity profile shall be measured using a certified ASTM standard procedure. Deviations from Gaussian behavior shall be considered when measuring beveled film thicknesses. Accounting for discrepancies from ideal behavior should result in increased accuracy of the technique.

Regarding the beveling phenomenon, results clearly show that there is a large variation in the bevel angle along a sidewall within a particular sputter crater. Deposition of a sacrificial overlayer has been moderately successful in effectively forcing layers of interest into the region of constant bevel angle along the crater sidewall. This approach has been attempted only on the p-HEMT device structure reported in this study. It shall be performed on other samples as well, and the improvement of measured film thicknesses as a result of sacrificial layer deposition will be evaluated. In addition, the uncertainty in the measurement of the bevel angle must be minimized. At present, the wide error bars associated with thickness measurements can be traced to the fact that the constant bevel angle is not unique. Different endpoints chosen along the central portion of the crater sidewall result in slightly different bevel angles, resulting in large uncertainties of film thicknesses. A standard procedure for determining the bevel angle must be developed before the technique can be reliably applied. Further investigation into standardizing bevel angle determination will be initiated.

Another issue which shall be addressed is the variability of bevel angle within the sidewall region of constant angle between different sputter craters. Expressed differently, for a particular sample, a deeper analysis crater results in an increased bevel angle. Initial results are encouraging in that the bevel angle dependence with sputter depth fits a linear function reasonably well, irrespective of the material. However, this phenomenon needs to be quantified in greater detail. A theoretical approach may be employed in which the Ar^+ beam

intensity profile is measured by the same manner in which the electron beam profile is measured. Once accomplished, intensity as a function of beam position is well known. Calculation yields ion beam current as a function of position at every point on the ion beam profile. Through the use of well documented ion sputter rates for different materials [22], the degree of differential sputtering along the crater sidewalls may be calculated. This, coupled with a knowledge of interatomic spacings for different materials, should enable one to theoretically map the crater sidewall as a function of lateral position. This will enable determination of an exact expression for the variable bevel angle as a function of crater depth. Such a procedure is attractive on theoretical grounds, but not practical due to beam mixing effects and drastic ion yield fluctuations between different materials in thin film device structures [18]. Furthermore, this exacting procedure would need to be performed on a virtually limitless class of materials; an unwieldy task. A more empirical approach is in order, in which select materials are experimentally studied for bevel angle dependencies with depth and subsequently compared to one another. This enables verification of the linear dependence of bevel angle on crater depth, and an accurate, numerically generated linear expression may be determined. In addition, the variation of bevel angle along the sidewall of one particular crater may be similarly investigated, yielding a least-squares polynomial describing crater depth vs. lateral position along the beveled sidewall. In this way, a database may be developed for a wide class of materials. The end result would be a lookup table of bevel angles for a number of materials at various sputter crater depths. Although a formidable task, such an approach is more practical than the theoretical alternative. Thus, an empirical study shall be undertaken to fully characterize the beveling phenomenon.

A more straightforward procedure for accurate assessment of the bevel

angle may be through the use of a two-circle optical goniometer, an instrument which measures shallow angles through optical reflectance techniques [41]. Instrument specifications state that a goniometer may measure angles to an accuracy of 0.05°, quite suitable for this application. However, a goniometer ideally measures the angle between two adjoining planes, and it has clearly been shown that the crater sidewall surface is characterized by a continuously varying angle. Due to this limitation, such a measurement may not provide the accuracy required for ultimately determining film thicknesses, but this is not presently known. Therefore, goniometer measurements shall be investigated as an alternative to measuring the shallow bevel angle.

Yet another available alternative for accurate determination of the bevel angle is modification of the electronic circuit which controls the Ar^+ ion beam rastering in the PHI660 scanning Auger microprobe. The modification shall be performed to yield a constant bevel angle during ion beam sputtering. Such an approach has been successfully implemented by McPhail and Dowsett [42] and also Hues, Makous, and Gillen [43]. This offers the advantage of precise computer control of the bevel angle of sputter craters. By such a method, bevel angle measurement is unnecessary because the angle is well known. In addition, angle variations within a specific crater are eliminated because the electronic rastering circuit maintains a constant sidewall angle throughout the entire crater. Therefore, the accuracy of the technique is increased due to elimination of error introduced through an additional processing step. Accurate measurement of layer thickness is thus ultimately determined by the accuracy of Auger line scanning used to measure the apparent film thickness. One degree of freedom has been eliminated from the technique. This approach offers great potential in refining the measurement technique and shall be attempted in the near future.

Much work remains in chemically etching sputter craters for resolution of

ultrathin layers. At present, only AlGaAs/GaAs and InGaAs/GaAs multiple quantum well systems have been studied. Appropriate etchants for other materials need to be determined. In addition, the effects of parameters such as etchant concentration and etching time shall be studied to obtain optimum conditions for resolving thin device layers. While chemical etching enhances resolution of thin layers, post-etched surfaces are observed to be quite rough. Etching-induced surface damage on remaining layers will be evaluated through scanning electron microscopy, optical microscopy, and Auger electron spectroscopy.

Through each of these studies, the accuracy and precision of measuring film thicknesses and qualitative resolution of thin films shall be improved. The final test for assessing accuracy is a comparison with TEM results. TEM shall be performed when applicable in order to observe accuracy improvements in the technique. The ultimate goal is a refinement of the technique to the point where thickness measurements with associated accuracies of ±10Å may be achieved. It is believed that such an expectation is attainable. Through this program of future studies, accurate thickness measurements of ultrathin layers will hopefully be achieved.

As a final note, a patent application has been filed on 28 February 1994 in the U.S. Patent and Trademark Office for measuring film thickness by the technique described in this thesis. The patent is entitled "Method for Measuring Thin Film Thickness," by Donald W. Eckart, Luis M. Casas, and Richard T. Lareau, serial number 8/204, 018.

REFERENCES

[1] R.L. Gieger, P.E. Allen, and N.R. Strader, *VLSI Design Techniques for Analog and Digital Circuits*, New York: McGraw-Hill, 1990, Chapter 1, pp. 4-10.

[2] Y. Okada, P.J. Tobin, P. Rushbrook, and W.L. DeHart, "The Performance and Reliability of 0.4 Micron MOSFET's with Gate Oxynitrides Grown by Rapid Thermal Processing Using Mixtures of N_2O and O_2," *IEEE Transactions on Electron Devices*, vol. 41, no. 2, pp. 191-197, 1994.

[3] I.C. Kizilyalli, M. Artaki, N.J. Shah, and A. Chandra, "Scaling Properties and Short-Channel Effects in Submicrometer AlGaAs/GaAs MODFET's: A Monte Carlo Study," *IEEE Transactions on Electron Devices*, vol. 40, no. 2, pp. 234-249, 1993.

[4] P.C. Chao, R.C. Tiberio, K.G. Duh, P.M. Smith, J.M. Ballingall, L.F. Lester, B.R. Lee, A. Jabra, and G.G. Gifford, "0.1-μm Gate Length Pseudomorphic HEMT's," *IEEE Electron Device Letters*, vol. EDL-8, pp. 489-491, 1987.

[5] G. Higashi, private communication.

[6] D.A. Buchanan, "Electrical Characterization of Thin Gate Insulators for sub 0.1 μm MOSFETs," presented at Advanced Technologies of Thin OxideFilms, Rutgers University, Piscataway, NJ, March 1994.

[7] J.M. Ballingall, Pin Ho, G.J. Tessmer, P.A. Martin, T.Y. Yu, P.C. Chao, P.M. Smith, and K.H.G. Duh, "Materials and Device Characteristics of Pseudomorphic AlGaAs-InGaAs-GaAs and AlInAs-InGaAs-InP High Electron Mobility Transistors," *Materials Research Society Symposium Proceedings*, vol. 160, *Layered Structures - Heteroepitaxy, Superlattices, Strain, and Metastability*, B.W. Dodson, L.J. Schowalter, J.E. Cunningham, and F.H. Pollak, Eds. Pittsburgh: Materials Research Society, 1990, pp. 759-770.

[8] M.O. Manasreh and G.J. Brown, *Semiconductor Quantum Wells and Superlattices for Long-Wavelength Infrared Detectors*, Boston: Artech House, 1993, Chapter 1, pp. 2-11.

[9] W.C. Liu, W.S. Lour, R.L. Wang, C.Y. Sun, and W.C. Hsu, "Application of GaAs-AlGaAs Superlattice Structure for Fabricating High Breakdown Voltage Power MISFET," *Materials Research Society Symposium Proceedings*, vol. 160, *Layered Structures - Heteroepitaxy, Superlattices, Strain, and Metastability*, B.W. Dodson, L.J. Schowalter, J.E. Cunningham, and F.H. Pollak, Eds. Pittsburgh: Materials Research Society, 1990, pp. 807-810.

[10] M.H. Herman, I.D. Ward, R.F. Kopf, S.J. Pearton, and E.D. Jones, "Characterization of Modulation Doped Pseudomorphic AlGaAs/InGaAs/GaAs HEMT Structures by Electron Beam Electroreflectance and Photoluminescence," *Materials Research Society Symposium Proceedings*, vol. 160, *Layered Structures - Heteroepitaxy, Superlattices, Strain, and Metastability*, B.W. Dodson, L.J. Schowalter, J.E. Cunningham, and F.H. Pollak, Eds. Pittsburgh: Materials Research Society, 1990, pp. 661-666.

[11] S. Lim, J.H. Ryu, J.F. Wager, and L.M. Casas, "Inhomogeneous Dielectrics Grown by Plasma-Enhanced Chemical Vapor Deposition," presented at the International Conference of Metallurgical Coating of Thin Films, San Francisco, CA, April 1993.

[12] M. Ohring, *The Materials Science of Thin Films*, New York: Academic Press, 1992, Chapter 6, pp. 249-306.

[13] S.A. Alterovitz, P.A. Sekula-Moise, R.M. Sieg, M.N. Drotos, and N.A. Bogner, "Ellipsometric Study of Metal-Organic Chemically Vapor Deposited III-V Semiconductor Structures," *Thin Solid Films*, vol. 220, pp. 241-246, 1992.

[14] R.C. Jaeger, *Introduction to Microelectronic Fabrication*, New York: Addison-Wesley, 1988, Chapter 6, pp. 117-128.

[15] W.Y. Han, M.W. Cole, L.M. Casas, A. DeAnni, M. Wade, K.A. Jones, A. Lepore, Y. Lu, and L.W. Yang, "Ohmic Contacts to p^+-GaAs and $Al_{0.26}Ga_{0.74}As$," presented at the 1994 Materials Research Society Spring Meeting, San Francisco, CA, April 1994.

[16] K.A. Jones, M.W. Cole, P. Cooke, J.R. Flemish, R.L. Pfeffer, and H. Shen, "Accurately Determining the Composition and Thickness of Layers in a GaAs/InGaAs Superlattice," to be published in the *Journal of Applied Physics*, May 1994.

[17] A.W. Agar, R.H. Alderson, and D. Chescoe, *Principles and Practice of Electron Microscope Operation*, New York: American Elsevier, 1974, Chapter 1, pp. 1-37.

[18] J.A. McHugh, *Methods and Phenomena 1: Methods of Surface Analysis*, Potsdam: Elsevier Scientific, 1975, Chapter 6, pp. 223-278.

[19] W.M. Riggs and M.J. Parker, *Methods and Phenomena 1: Methods of Surface Analysis*, Potsdam: Elsevier Scientific, 1975, Chapter 4, pp. 103-158.

[20] S. Wolf and R.N. Tauber, *Silicon Processing for the VLSI Era, Volume 1: Process Technology*, Sunset Beach: Lattice Press, 1986, Chapter 17, pp. 586-617.

[21] A. Joshi, L.E. Davis, and P.W. Palmberg, *Methods and Phenomena 1: Methods of Surface Analysis*, Potsdam: Elsevier Scientific, 1975, Chapter 5, pp. 159-222.

[22] R.G. Wilson, F.A. Stevie, and C.W. Magee, *Secondary Ion Mass Spectrometry: A Practical Handbook for Depth Profiling and Bulk Impurity Analysis*, New York: Wiley, 1989, Chapter 3, pp. 2-1 - 2-13.

[23] L.E. Davis, N.C. MacDonald, P.W. Palmberg, G.E. Riach, and R.E. Weber, *Handbook of Auger Electron Spectroscopy*, Eden Prairie: Physical Electronics Industries, 1978.

[24] J.M. Morabito and R.K. Lewis, *Methods and Phenomena 1: Methods of Surface Analysis*, Potsdam: Elsevier Scientific, 1975, Chapter 7, pp. 279-328.

[25] D.G. Rickerby, "Low Voltage Field Emission SEM and Microanalysis of Multilayer Films," *Microscopy and Analysis*, issue 4, pp. 11-13, 1994.

[26] R.T. Lareau, private communication.

[27] R.E. Hummel, *Electronic Properties of Materials: An Introduction for Engineers*, New York: Springer-Verlag, 1985, Chapter 7, pp. 67-71.

[28] G.K. Wehner, *Methods and Phenomena 1: Methods of Surface Analysis*, Potsdam: Elsevier Scientific, 1975, Chapter 1, pp. 5-37.

[29] James Bheam, private communication.

[30] D.W. Eckart and L.M. Casas, "Shallow Angle Beveling of Thin Layer Structures by an Ion Beam/Chemical Etching Technique," *Applied Physics Letters*, vol. 63, no. 8, pp. 1041-1043, 1993.

[31] S.N. Schauer, L.M. Casas, A.E. Souzis, R.T. Lareau, and P. Li Kim Wa, "Analysis of Zn-Diffused MQW Waveguides Using SIMS and AES," presented at the Sixth East Coast Workshop on Secondary Ion Mass Spectrometry, Hopewell Junction, NY, May 1993.

[32] J.E. Freund and R.E. Walpole, *Mathematical Statistics*, Englewood Cliffs: Prentice-Hall, 1987, Chapter 6, pp. 221-226.

[33] M.W. Cole, private communication.

[34] H.D. Young, *Statistical Treatment of Experimental Data*, New York: McGraw-Hill, 1962, Chapter 1, pp. 9-18.

[35] G.B. Thomas, Jr. and R.L. Finney, *Calculus and Analytic Geometry*, Reading: Addison-Wesley, 1984, Chapter 15, pp. 811-817.

[36] T.J. Hoover, private communication.

[37] H.S. Lee, M.W. Cole, R.T. Lareau, L.M. Casas, R.J. Thompson, A. DeAnni, K.A. Jones, W.Y. Han, Y. Lu, and L.W. Yang, "Ohmic Contacts to Heavily Carbon-Doped p^+-GaAs Using Ti/Si/Pt," presented at the 18th Army Science Conference, Orlando, FL, June 1992.

[38] S. Lim, private communication.

[39] N.M. Ravindra, F.M. Tong, S. Amin, J. Shah, W.F. Kosonocky, N.J. McCaffrey, C.N. Manikopoulos, B Singh, R. Soydan, L.K. White, P. Zanzucchi, D. Hoffman, R.T. Lareau, L.M. Casas, T. Monahan, and D.W. Eckart, "Development of Emissivity Models and Induced Transmission Filters for Multi-Wavelength Imaging Pyrometry (M-WIP)," presented at Thermosense XVI, Orlando, FL, April 1994.

[40] G.R. Fox, S. Trolier-McKinstry, S.B. Krupanidhi, and L.M. Casas, "Pt/Ti/SiO2/Si Substrates," to be published in *Thin Solid Films*, 1994.

[41] D.W. Eckart, private communication.

[42] D.S. McPhail and M.G. Dowsett, "Bevelling-Etching-Imaging - A Novel Technique for Resolving Thin Layer Structures," *Proceedings of SIMS VI*, A. Benninghoven, A.M. Huber, and H.W. Werner, Eds. New York: Wiley, 1987, pp. 269-272.

[43] S.M Hues, J.L. Makous, and G Gillen, "The Application of SIMS Bevel Depth Profiling to Al-Doped Mo/Ni Superlattice Films," *Proceedings of SIMS VIII*, A. Benninghoven, K.T.F. Janssen, J. Tumpner, and H.W. Werner, Eds. New York: Wiley, 1992, pp. 745-748.